10-27-2017

# Overbank Deposition of Sand and Mud within Two Point Bars Bound by the Mississippi River Levee System: Implications for Coastal Restoration Sediment Budgets

Christopher Magliolo
*Louisiana State University and Agricultural and Mechanical College*

# OVERBANK DEPOSITION OF SAND AND MUD WITHIN TWO POINT BARS BOUND BY THE MISSISSIPPI RIVER LEVEE SYSTEM: IMPLICATIONS FOR COASTAL RESTORATION SEDIMENT BUDGETS

A Thesis

Submitted to the Graduate Faculty of the
Louisiana State University and
Agricultural and Mechanical College
in partial fulfillment of the
requirements for the degree of
Master of Science

in

The Department of Geology and Geophysics

by
Christopher Ryan Magliolo
B.S. Louisiana State University, 2015
December 2017

**ACKNOWLEDGMENTS**

I would like to begin by thanking my thesis advisor, Professor Samuel J. Bentley of the Department of Geology and Geophysics and Associate Dean for Research and Administration in the College of Science at Louisiana State University. His expertise and support through this project, as well as a belief in my abilities provided the latitude to accomplish this project. I am grateful for his guidance throughout my undergraduate and graduate career. The Louisiana Coastal Protection and Restoration Authority was instrumental in the completion of this project by providing the funding and grant support to conduct this project. I hope that the trust and confidence granted by the agency will lead to answers related the vital interests of the State of Louisiana and the Coastal Master Plan. My thesis committee, consisting of Professor Peter Clift and Assistant Professor Carol Wilson, also provided key support during the analysis and writing of this thesis.

To the Marines of 3d Force Reconnaissance Company, with whom I continue to serve – you are the finest examples that being a great warrior does not prevent one from being a good man.

A number of students in Dr. Bentley's lab, including Crawford White, Giancarlo Restreppo, Jeff Bomer, Ryan Clarke, Pat Baudoin, Brianna Crenshaw, and Suyapa Gonzales, assisted in the field campaign and provided peer guidance throughout the project. Without the LSU Coastal Studies Institute boat shop, this project would not have been possible. Mr. DeWitt Braud provided key insight for the spatial analysis involved in this project. Thanks goes to a number of local landowners, State Representative Kenneth Havard, the US Department of the Interior, the Nature Conservancy, and The Roy O. Martin Company who provided land access for core collection.

Finally, I dedicate this thesis and the efforts put forth in its accomplishment to my wife Sarah and our four children, Braden, Ian, Ava Sophia, and Augustin. I am grateful for your love and patience. The work is nearly done.

**TABLE OF CONTENTS**

## LIST OF TABLES

## LIST OF FIGURES

**Figure 30.** Analysis of the mass accumulation rates of all cores. Based on distance (a) shows that MARs changed by -6.69 x $10^{-5}$ g $cm^{-2}$ $y^{-1}$ for every meter of distance away from the river or oxbow lake ($r^2$ = 0.06). Based on elevation (b), MARs changed by 0.142 g $cm^{-2}$ $y^{-1}$ ($r^2$ = 0.32) for every meter of elevation gained.

**Figure 31.** Analysis of the mass accumulation rates of cores taken from the east bank (Cat Island). Based on distance (a), MARs changed by -1.34 x $10^{-4}$ g $cm^{-2}$ $y^{-1}$ for every meter of distance away from the river or oxbow lake ($r^2$ = 0.34). Based on elevation (b), MARs changed by 0.139 g $cm^{-2}$ $y^{-1}$ ($r^2$ = 0.36) for every meter of elevation gained.

**Figure 32.** Analysis of the mass accumulation rates of cores taken from Raccourci Island (west bank). Based on distance (a), MARs changed by 3.061 x $10^{-4}$ g $cm^{-2}$ $y^{-1}$ for every meter of distance away from the river or oxbow lake ($r^2$ = 0.45). Based on elevation (b), MARs changed by 0.191 g $cm^{-2}$ $y^{-1}$ ($r^2$ = 0.31) for every meter of elevation gained.

**Figure 33.** Sediment storage reservoirs in the study area include: 1) east bank, 2) west bank, 3) Raccourci Old River lakeshore, 4) Cat Island, and 5) Raccourci Island.

**Figure 34.** Analysis of the mass accumulation rates of cores taken near open water channels. MARs changed by 0.0028 g $cm^{-2}$ $y^{-1}$ for every meter of increased distance ($r^2$ = 0.52).

**Figure 35.** Analysis of the mass accumulation rates of cores taken inland on the point bars. MARs changed by 0.258 g $cm^{-2}$ $y^{-1}$ for every meter of elevation gained ($r^2$ = 0.61).

**Figure 36.** Based on elevation changes, these are the expected mass accumulation rates throughout the inland portions of the study area. The portions of the point bars nearest the Mississippi River and Raccourci Old River are highlighted in light blue. Results are included above in Table 16.

**Figure 37.** (a-f) Growth of The Narrows sand bar and lacustrine delta complex infills Raccourci Old River from 1998-2014. The square marker indicates the coring location of Core FP-RI-NRW. (g) The final overhead imagery frame, taken in November 2015, shows the impending emergence of the coring location above the surface of the lake.

**ABSTRACT**

As ongoing Mississippi River sediment diversion projects are being developed and planned, the availability of sand and mud for use in the lower Mississippi River Delta is being calculated and budgeted. This project attempts to quantify the amount of sand and mud being lost from the lower Mississippi River past the Old River Control Structure in the remaining unleveed floodplains, an area that encompasses 270 $km^2$. Two land masses were chosen along each bank of this reach of the Mississippi River: Raccourci Island (west bank) and the Cat Island National Wildlife Refuge (east bank). Seventeen sediment cores were collected and have been analyzed for the presence of Cesium-137, a radioactive isotope that resulted from the fallout of nuclear weapons testing, and Lead-210, a natural Uranium-series radioisotope. Cores were also analyzed for grain size and bulk density. The combined geochronological, grain size, and density results allow the spatial distribution of sediment mass accumulation rates to be determined, and a key motivation of this project is to ascertain how much sediment is being trapped annually by these floodplains that retain a natural connection to the river.

Sediment accumulation rates ranged from 0.217 to 1.04 cm $yr^{-1}$. Conversion of sediment accumulation rates to mass accumulation rates was conducted and resulted in a range of 0.073 to greater than 1.48 g $cm^{-2}$ $yr^{-1}$. A regional mass accumulation rate was determined using natural neighbor interpolation and characterizing deposition according to geography and topography. These methods were based on elevation for cores greater than 500 meters from open water and based on distance from a channel for cores within 500 meters of an open channel. A range of total sediment mass loss was calculated to be 1.58 to 3.03 MT $yr^{-1}$. Additional pathways for sediment storage in the region include growth of the Narrows lacustrine delta and an additional 82 $km^2$ of unleveed floodplains and river islands south of Saint Francisville to Baton Rouge. The estimated

sediment storage to these two pathways are 0.45 and 0.64 MT $yr^{-1}$, respectively, for a final total range of 2.46 to 4.27 MT $yr^{-1}$.

# 1. INTRODUCTION

## 1.1 Background

The Mississippi River Delta has experienced a sediment load decrease of at least 50% (Kesel et al, 1992) with advent of flood protection measures built in the region in the last 90 years (Blum and Roberts, 2009). The damming of major tributaries to the Mississippi River has decreased sediment delivery to the lower Mississippi River Delta resulting in much decreased sediment supply to southeastern Louisiana. Additional flood protection measures include course changes, river flow control structures, and the construction of flood protection levees. Acceleration of natural subsidence has also occurred locally; collectively these factors have contributed to a loss of 5,000 $km^2$ of deltaic wetlands in the Mississippi River Delta, or approximately 25% of the total area, which have reverted to open water (Day et al, 2007). Mississippi River Delta restoration projects are crucial in addressing this loss. Funding for such action has become a growing priority (LA CPRA, 2017). A critical question has been posed regarding the amount of sediment that is available in the Mississippi River for key restoration projects that aim to build river sediment diversions that would allow sediment to reach the delta once again. It has been estimated that sustainment of the existing delta would require 18-24 billion tons of sediment over decadal to centennial timescales (Blum and Roberts, 2009).

Allison, et al. (2012) studied sediment delivery along the Mississippi River downstream of the Old River Control Structure and north of Saint Francisville, Louisiana, and determined that 15.9 MT $yr^{-1}$ of mud and 53.8 MT $yr^{-1}$ of sand were lost from transport during a three year period. The reason for this loss was not known, but hypothesized to be due to two primary factors, bed aggradation and overbank deposition. An additional 7.9 MT $yr^{-1}$ of mud were lost along the stretch between Saint Francisville and Baton Rouge (Allison et al, 2012). Bentley et al. (2015) estimated

that this mass of sediment, if deposited as a layer of uniform thickness along this reach, would produce bed aggradation an order of magnitude greater than that presently observed in data collected by the United States Corps of Engineers (US-ACE, 2014), suggesting that bed aggradation is not the primary sink for the missing sediment. A pilot study conducted by Smith and Bentley (2014) focused on overbank deposition and attempted to quantify sediment accumulation rates in Cat Island National Wildlife Refuge. Using four cores, mass accumulation rates ranged from 0.31-1.11 g $cm^{-2}$ $yr^{-1}$ with an average of 0.49-0.73 g $cm^{-2}$ $yr^{-1}$. A maximum regional mass accumulation rate of 1.64-2.11 MT $yr^{-1}$ was calculated for the 270 $km^2$ study area, accounting for 10-13% of the total annual suspended load sediment lost determined by Allison et al (2012). These results were included in this study to aid in the development of a new regional mass accumulation rate. In response to these initial results and the large degree of uncertainty, the Louisiana Coastal Preservation and Restoration Authority requested that a more detailed study be conducted with a larger data set covering both banks of the Mississippi River (Smith and Bentley, 2014).

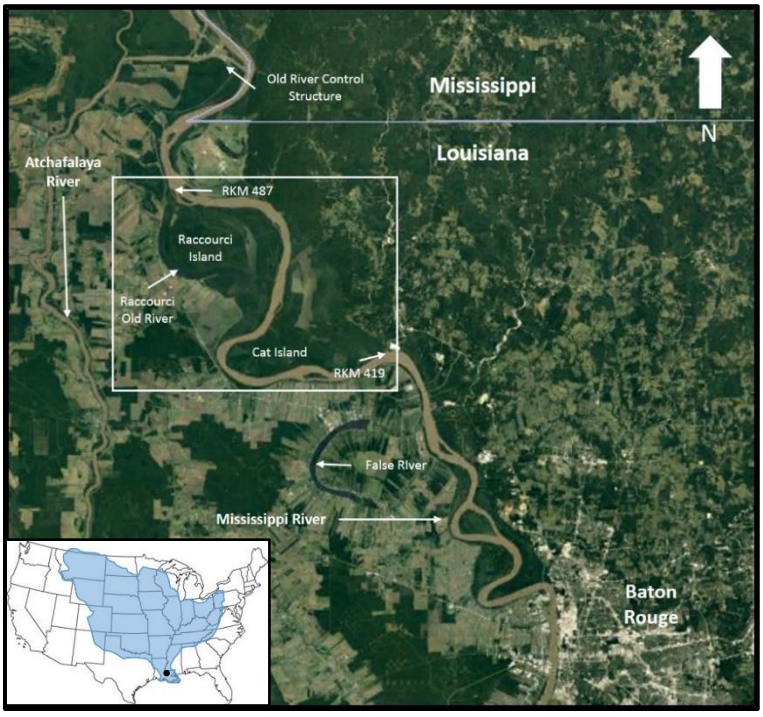

**Figure 1.** Regional overview from the Old River Control Structure to Baton Rouge, Louisiana (Image source: Google Earth, *Landsat*). Inset – Watershed of the Mississippi River. The study area is indicated by the black circle. (Adapted from National Park Service).

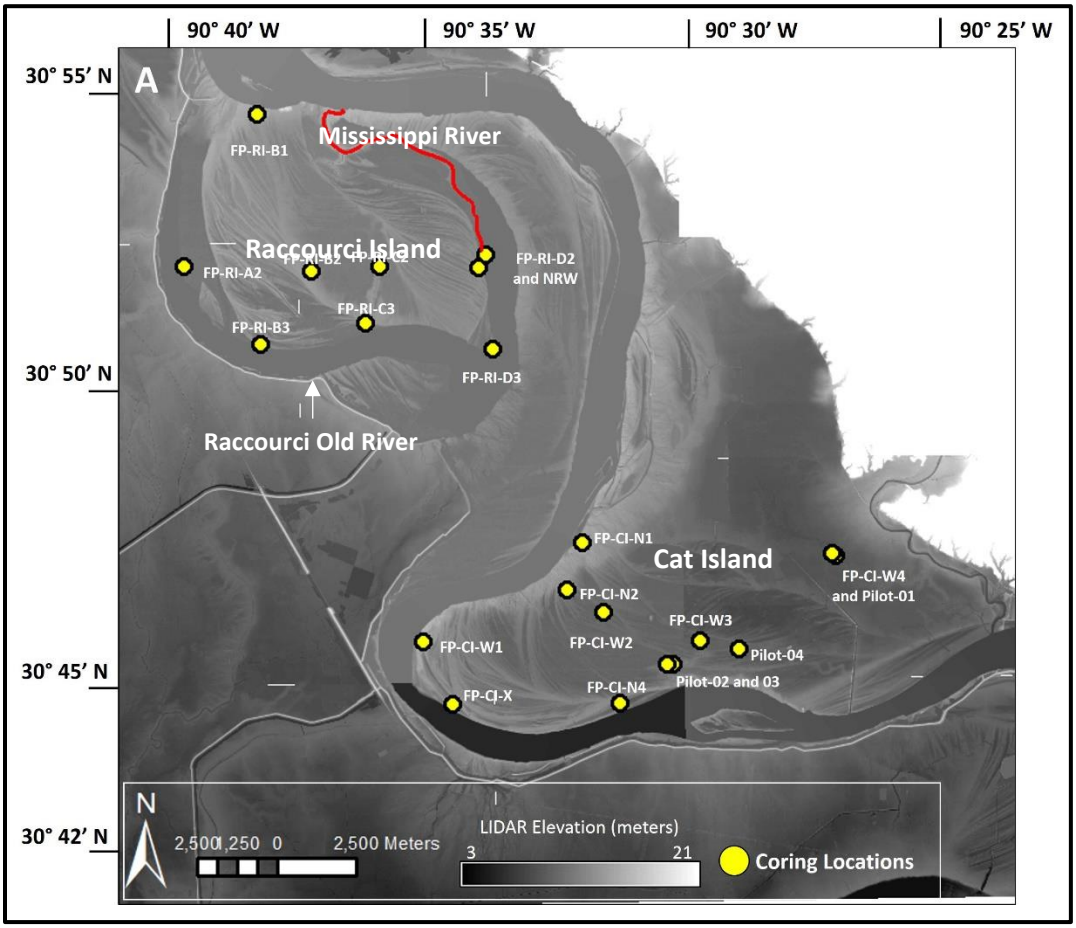



**Figure 2.** (a) Greyscale LIDAR imagery illustrating the study areas: Cat Island, Raccourci Island, and Raccourci Old River. The red path indicates the path of the tie channel known as The Narrows (Image source: Louisiana Atlas website, accessed April 2017). (b) The tie channel known as The Narrows is a 9 km channel that connects the Mississippi River to Raccourci Old River (Image source: Google Earth, *Landsat*).

At the Old River Control Structure, the Mississippi River bifurcates into a main channel and the largest distributary, the Atchafalaya River. Along the reach of the Mississippi River beginning at river kilometer (RKM) 487 at the Old River Control Structure and ending at RKM 419 at Saint Francisville, Louisiana (Figures 1 and 2), the unleveed floodplain encompasses a region of approximately 270 $km^2$. Two Mississippi River point bars/island complexes, Raccourci Island and Cat Island, are located on the first and second meanders beyond the Old River Control Structure, and upstream of Saint Francisville. This is the floodplain region that could serve as a depositional sink highlighted by Allison et al. (2012), Smith and Bentley (2014), and Bentley, et al. (2015).

**1.2 Point Bar Development**

Both Raccourci Island and Cat Island are Mississippi River point bars that developed as a series of scroll bars accreted onto meanders located on the east bank of the Mississippi River (Figures 1-3). Development of these scroll bars progressed via a bank pull mechanism as outer banks on a river meander erodes and channels widened. Evidence of this development can be observed by the ridge and swale pattern that has left a series of periodically inundated sloughs visible in satellite imagery and Light Detection and Ranging (LIDAR) imagery (Figure 2a). The individual ridges represent preserved older point bar surfaces while the individual swales represent former channel chutes that develop between the bank and the bar. The sloughs, or swales, have been demonstrated to retain finer grained material (van de Lageweg et al, 2014).

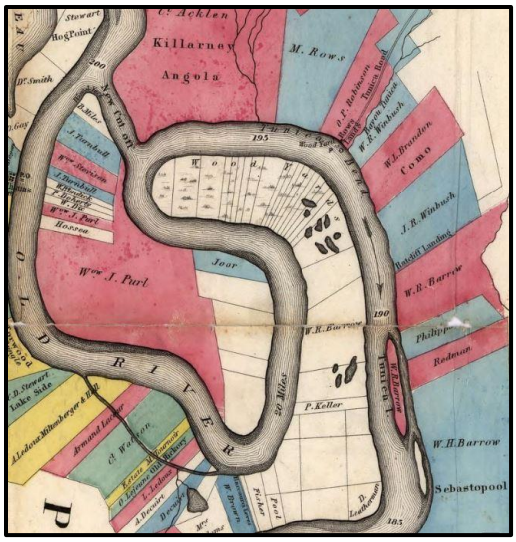


**Figure 3.** Development of Raccourci Island occurred after a canal was cut across the thin isthmus at the northwest portion of the shortening the Mississippi River by approximately 30 km (Photo credit: Norman, 1858 Chart of the Lower Mississippi River, Library of Congress Website, accessed April 2017).

Raccourci Island (Figures 2a, 3) was created in the mid-19th century by means of an artificial cut designed to shorten the course of the Mississippi River by more than 30 km. This cut was achieved by digging a shallow trench that captured the river (Rowland, et al, 2005). Through the natural action of river erosion and chute channel development, the trench increased in width and depth until a cutoff developed across the old bar (Figure 3). Over time, the original channel was infilled on the eastern and western edges of the cutoff until an oxbow lake, Raccourci Old River, formed. Today, the western edge of the original channel is completely infilled. On the eastern edge of the cutoff, a tie channel, known as The Narrows developed and now extends more than nine km into the original channel. It continues to actively prograde as a lacustrine delta into Raccourci Old River. The Raccourci Island point bar was originally situated on the east bank of the Mississippi River, and it remains in West Feliciana Parish, rather than Pointe Coupee Parish, located on the west bank (Rowland, et al, 2009).

The oxbow lake, Raccourci Old River, has a total area of 19.35 $km^2$ and remains connected to the main stem of the Mississippi River via The Narrows (Rowland, et al, 2009) (Figure 2b). Currently, Raccourci Island is 61 $km^2$ and is privately owned land containing hunting camps, and bottomland forests managed for lumber harvesting. An additional unleveed area of 65 $km^2$ is located on the peninsula located between Raccourci Old River and the west bank of the Mississippi River.

Cat Island (Figure 2a) is situated on the east bank floodplain of the Mississippi River consisting of 144 $km^2$. To its east, it is bound by the uplands of Tunica Hills and Bayou Sara, a natural waterway flowing into the Mississippi River. Cat Island begins at RKM 459 and is located to the southeast of Raccourci. Currently, Cat Island contains private land, a private nature preserve managed by The Nature Conservancy, and the Cat Island National Wildlife Refuge, managed by United States Department of the Interior (US Fish and Wildlife Service, 2015).

Both study areas are characterized as woody wetlands that are located within the manmade levee system built and maintained by the US Army Corps of Engineers. Cat Island remains outside of the levee system as no construction was necessary in the highlands near Saint Francisville. Since Raccourci Island was originally situated on the east bank of the Mississippi River, the west bank levees were built up along the original west bank along what is now the southern edge of Raccourci Old River. These floodplains allow for increased water storage capacity as the Mississippi River rises each year due to flooding. In the past, this increased water storage capacity has aided in limiting the number of times the floodgate mechanisms at the Morganza Floodway and the Bonnet Carre' Spillway are required to be opened. Current standing instructions allow for the opening of the floodgates in order to release water temporarily stored in the forebay of the Morganza Floodway (US-ACE, 2014). As a result, these two areas serve as a small-scale analog to the larger

historical floodplains that were present along the Mississippi River prior to construction of the levee system (Smith and Bentley, 2014).

In order to define permanent sediment loss and storage for the scope of the project, identification of storage sinks is required. During periods of low river flow, exposed sand bars with no vegetation can be observed extending away from point bars and river islands further into the river. Since the sediments deposited in these areas are readily transported during periods of high river flow, these river point bars were not included in this project's investigation. For the scope of this project, the focus is on sediment deposition occurring in the form of vertical aggradation during overbank flooding. The current regimen of suspended sediment deposition via overbank flooding captures mostly mud, especially at greater distances from the river channel; additionally, the swales are expected to contain sediment of further decreased grain size (van de Lageweg et al, 2014).

### 1.3 Flooding Events

While the focus of investigation for this study is overbank deposition through periodic flooding, inclusion of other mechanisms for sediment deposition along this reach have been considered. Rowland, et al (2009) investigated the Narrows tie channel feeding Raccourci Old River in depth and determined lacustrine-deltaic sedimentation produced a sediment bar prograding into Raccourci Old River since re-routing the river in the 1800s. Under these conditions, Rowland, et al (2009) estimated that 450,000 tons $yr^{-1}$ were captured as a lacustrine delta over the course of 150 years (Rowland, et al, 2009).

Overbank flooding along this reach occurs when the Mississippi River rises above its flood stage of 14.63 meters as measured at Red River Landing. Three flooding events occurred during this study. Inundation depths reached more than two meters in both field areas. In addition to the

three flooding events that occurred during the study period, 24 total flooding events have occurred since the year 2000 (Table 1, Figure 4). Of these 24 events, nine significant flooding events occurred. These events are characterized in this study as those of a duration greater than 30 days or when cresting surpassed 16.75 meters (US Army Corps of Engineers website, 2017).

**Table 1.** Mississippi River flooding events from 2000-2017, including three events (starred) that occurred during the course of this study.

| Flooding Event | Duration (days) | Maximum River Crest (m) |
|---|---|---|
| January 2005 | 30 | 16.79 |
| March 2009 | 75 | 18.50 |
| May 2009 | 38 | 17.65 |
| May 2011 | 60 | 19.21 |
| May 2013 | 59 | 16.16 |
| March 2015 | 52 | 16.25 |
| June 2015* | 71 | 17.10 |
| January 2016* | 39 | 16.98 |
| March 2016* | 35 | 16.98 |

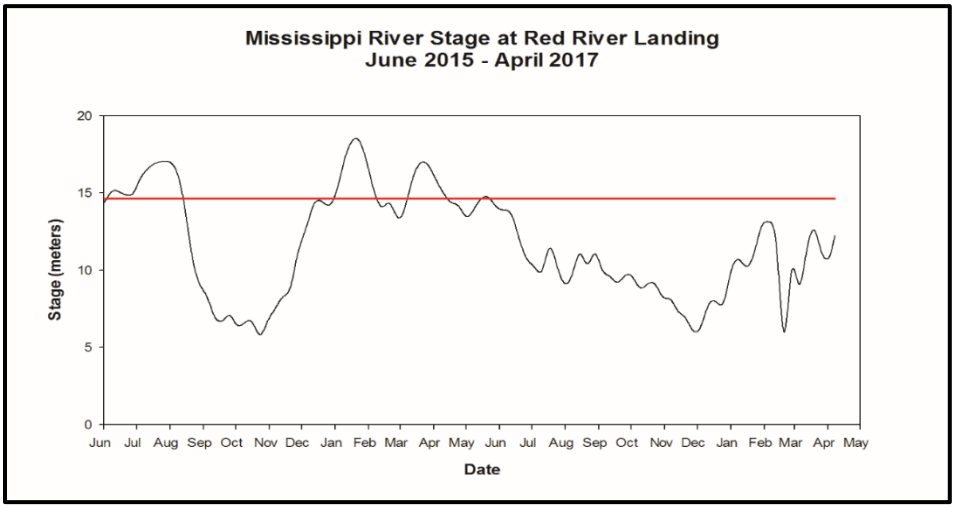


**Figure 4.** Mississippi River weekly stage taken over the course of the study period. Flood stage at Red River Landing (indicated with red line above) is measured at 14.63 m. Three significant flooding events occurred during this timeframe (Adapted from river gage data collected by the US-ACE New Orleans District, *http://rivergages.mvr.usace.army.mil*).

The key hypotheses guiding this project include: Overbank flooding deposition will be dominated by fine-grained sediment with the presence of coarser-grained being present closer to the main channel. Consequently, the sediment of increased grain size and higher sediment accumulation rates (cm $yr^{-1}$) are expected along the natural levees. Additionally, it is expected that

within the areas of lower topographic relief, decreased grain size and increased total organic content will be observed.

## 2. METHODS

### 2.1 Core Collection and Processing

The two field study areas were accessed by four-wheel drive vehicles, ATVs, and on foot. During low-water periods, eight cores were collected from Cat Island and nine cores were collected from Raccourci Island, for a total of 17 cores (Figures 5 and 6). Locations were chosen based on preliminary north-south and west-east transects created using Google Earth Pro. A final determination for each location was made in the field using the factors of accessibility to roads, distance from adjacent points, and distance from the Mississippi River channel and Raccourci Old River. Transects on Cat Island and Raccourci Island formed a rough grid. The cores came from a variety of environments including the natural levee, bottomland forest, and the subaqueous nearshore lake bed. In two locations on the west bank (Figure 7), cores were taken in a subaqueous environment using 7.62-cm vinyl push cores. Though these cores were located in a subaqueous environment at the time of collection, both locations are subject to exposure in subaerial conditions as seasonal evaporation occurs. Additionally, these locations were close enough to the exposed point bars that they would be poor candidate locations for deep-water coring locations since they are periodically above water and were collected in less than three meters of water depth. These cores were capped and sealed for transport. Core locations were determined with hand-held GPS and ground elevation at each sampling location was estimated from LIDAR data (Tables 2 and 3).

Remaining terrestrial cores were collected using a 5.7-cm diameter, 1.2-m long gouge auger core sampler (AMS, Inc. American Falls Idaho) with a semi-cylindrical profile, approximately 60% of a circle's circumference. The coring device was hand-driven into the ground and rotated in order to retrieve a core made up of a full circle. The use of the hand-driven coring devices is designed to minimize compaction of sediment in the core.

Each terrestrial core was wrapped and sealed in the field in plastic wrap, and transported in a 6-cm PVC tube split along its length. The volume of sediment recovered after extraction from the auger is generally less than a full cylinder, owing to core design. To estimate the volume of sediment recovery, sample volumes were adjusted throughout the depth of each core using the following formula:

$$Total\ Sample\ Volume = Retrieved\ \% * \pi * (Core\ Radius)^2 * Thickness \quad (1)$$

As described below, each core was measured in the lab and analyzed in the laboratory at 2-cm intervals for: radioisotope activity, total organic content, and granulometry.

**Table 2.** Core classification and locations along the Cat Island transects. Elevations derived from State of Louisiana LIDAR digital elevation models at 5 m planar and 0.61 m vertical resolution.

| Core Name | Core Classification | Latitude | Longitude | Elevation (meters) |
|---|---|---|---|---|
| FP-CI-N1 | Natural Levee | 30°47'21"N | 091°31'59"W | 15.21 |
| FP-CI-N2 | Bottomland | 30°46'33"N | 091°32'18"W | 11.37 |
| FP-CI-N4 | Bottomland | 30°44'37"N | 091°31'16"W | 10.34 |
| FP-CI-X | Bottomland | 30°44'38"N | 091°34'34"W | 11.68 |
| FP-CI-W1 | Natural Levee | 30°45'42”N | 091°35'08"W | 14.26 |
| FP-CI-W2 | Bottomland | 30°46'10"N | 091°31'34"W | 10.38 |
| FP-CI-W3 | Bottomland | 30°45'48"N | 091°29'47"W | 11.09 |
| FP-CI-W4 | Bottomland | 30°47'05"N | 091°27'01"W | 9.96 |
| Pilot-01 | Bottomland | 30°47’06” | 091°27’04”W | 9.51 |
| Pilot-02 | Bottomland | 30°45’16”N | 091°30’13”W | 12.62 |
| Pilot-03 | Bottomland | 30°45’15”N | 091°30’20”W | 11.20 |
| Pilot-04 | Bottomland | 30°45’30”N | 091°28’55”W | 10.30 |

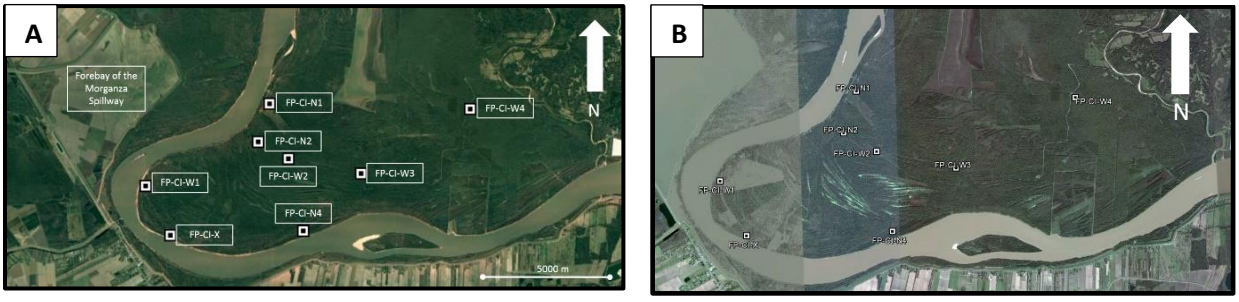


**Figure 5.** Coring locations on Cat Island. Imagery shows a comparison of (a) low water and (b) flooding. (Image source: Google Earth, *Landsat*; Imagery Dates: a) Dec 2014, b) Dec 2015).

**Table 3.** Core classification and locations along the Raccourci Island transects. Elevations derived from State of Louisiana LIDAR digital elevation models at 5 m planar and 0.61 m vertical resolution.

| Core Name | Core Classification | Latitude | Longitude | Elevation (meters) |
|---|---|---|---|---|
| FP-RI-A2 | Subaqueous | 30°52'07"N | 091°39'45"W | 11.65 |
| FP-RI-B1 | Natural Levee | 30°54'41"N | 091°38'16"W | 15.23 |
| FP-RI-B2 | Bottomland | 30°52'01"N | 091°37'14"W | 12.11 |
| FP-RI-B3 | Natural Levee | 30°50'46"N | 091°38'16"W | 12.27 |
| FP-RI-C2 | Bottomland | 30°52'04"N | 091°35'53"W | 12.68 |
| FP-RI-C3 | Natural Levee | 30°51'07"N | 091°36'11"W | 12.38 |
| FP-RI-D2 | Natural Levee | 30°52'05"N | 091°33'56"W | 13.57 |
| FP-RI-D3 | Natural Levee | 30°50'39"N | 91°33'41"W | 11.43 |
| FP-RI-NRW | Subaqueous | 30°52'15"N | 091°33'48"W | 11.37 |

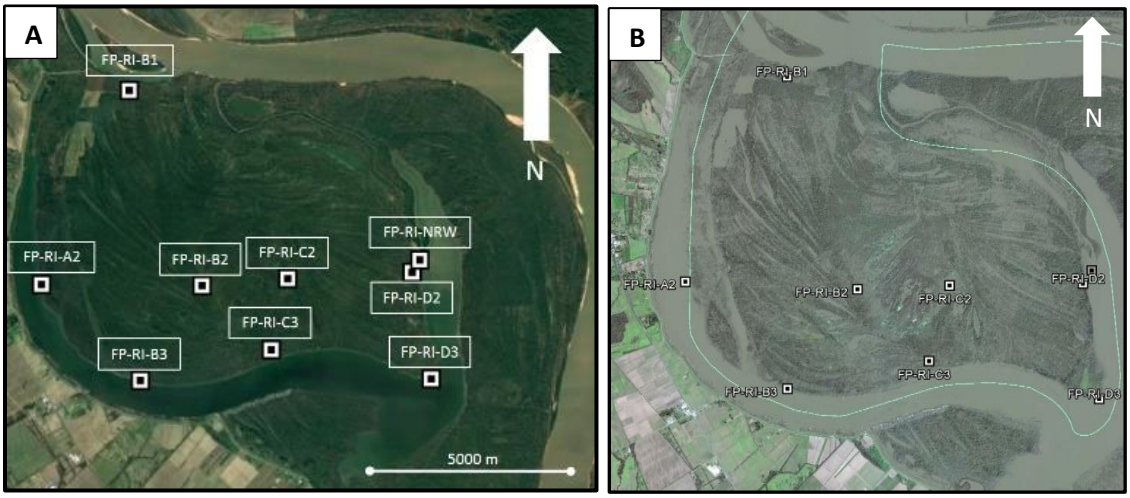


**Figure 6.** Coring locations on Raccourci Island. Imagery shows a comparison of (a) low water and (b) flooding. (Image source: Google Earth, *Landsat*; Imagery Dates: a) Dec 2014, b) Dec 2015).

## 2.2 Total Organic Content and Dry Mineral Density Analysis

Total organic content was determined using the loss on ignition method. Using a sub-sample from each 2-cm depth interval, all organic content was burned in a muffle furnace at 550° C for at least four hours leaving only the remaining mineral sediment portion (Heiri, et al, 2001). A digital scale capable of measuring samples to 0.1 mg recorded the sub-sample's dry mass and the sub-sample's post-burn mass. Upon completion of the burn, the remaining dried portions from core samples will be retained in a 60°C oven for cooling prior to measurement. The following formulae

were used to determine the percentage of organic content and to develop a dry mineral density formula:

$$Organic\ Mass\ \ Fraction = \frac{(Sample\ Dry\ Mass - Sample\ Burn\ Mass)}{Sample\ Dry\ Mass} \quad (2)$$

$$Dry\ Mineral\ Fraction = 1 - \ Organic\ Mass\ Fraction \quad (3)$$

The sample volume, wet mass, dry mass, total organic content of each sample was used to determine dry mineral density (i.e., dry bulk density after removal of organics). Dry mineral density for each core and core sample was calculated using the following formula:

$$Dry\ Mineral\ Density = (\frac{Dry\ Mass}{Total\ Sample\ Volume}) * Dry\ Mineral\ Fraction \quad (4)$$

Dry mineral density was used to convert sediment accumulation rates to mass accumulation rates.

**2.3 Development of Sediment Accumulation Rates Using Radiochemistry**

The radionuclides Cesium-137 ($^{137}$Cs, $t_{1/2}$ = 30.1 years, photopeak at 661 keV) and Lead-210 ($^{210}$Pb, $t_{1/2}$ = 22.2 years, photopeak at 46.5 keV) were used to determine the sediment accumulation rates (SARs). The photopeak of each radionuclide can be measured simultaneously via gamma spectroscopy in a high-resolution geranium gamma detector (Nittrouer et al, 1983; Corbett and Walsh, 2015).

Cesium-137 is a manmade radioactive isotope that resulted from the atmospheric fallout of nuclear weapons testing and leakage from nuclear power plants. Cesium is readily adsorbed onto clay or organic particles, however it can still be measured on coarser materials such as coarse silt or fine-grained sand. The radioisotope $^{137}$Cs serves as a worldwide marker in the sediment column that can be observed as early as 1954 and exhibits its highest activity and concentrations at the year 1963 (Hardy, 1971; Chmura and Kosters, 1994, Ritchie and McHenry, 1990). Following the suspension of atmospheric nuclear testing, the concentrations of $^{137}$Cs in the atmosphere and the

sediment column decreased dramatically. The 1963 peak is observed as a sharp peak at the profile's highest activity. Below the highest activity, the profile trails off to zero representing 1954. Therefore, each of the marker years are effective in developing a geochronology for the past 54 and 63 years. (Corbett and Walsh, 2015).

Lead-210 is a naturally occurring Uranium-series radioisotope also used for geochronology. It is an intermediate daughter isotope produced as radioactive $^{238}$U decays to stable $^{206}$Pb (see decay series below). Its mode of deposition is through atmospheric fallout via rainfall, dry deposition, or via settling through a water column. $^{210}$Pb is useful for developing age models potentially up to >100 years, depending on sediment type and other factors (Corbett and Walsh, 2015).

$$^{238}U \rightarrow {}^{226}Ra \rightarrow {}^{222}Rn \rightarrow {}^{210}Pb \rightarrow {}^{210}Po \rightarrow {}^{206}Pb$$

Unlike many locations for many studies conducted utilizing $^{137}$Cs and $^{210}$Pb, the study areas herein are not always underwater. Appleby (2008) investigated a number of desert lakes subject to evaporation and high variance in rainfall. Similarly, the wetlands in the study areas investigated in this project receive fallout via rainfall and periodic flooding followed by water drainage and evaporation. Each of the radionuclides utilized in the study have been shown to be sufficient tools in geochronology construction in circumstances where inundation is not constant, and are applicable in this study as well (Appleby, 2008).

The dried samples were broken and homogenized into a fine powder of mineral grains and organics manually using a mortar and pestle. A portion of the sample, the radionuclide count mass, was sealed with hot glue in a 50 mm x 9 mm petri dish.

When possible, the peak activity level for $^{137}$Cs was identified and correlated to 1963. Then the earliest observable activity was identified and correlated to 1954. If this method was possible, the average of the two sediment accumulation rates was taken. If this method was not possible, the

baseline activity detected at the year 1954 was used (Smith and Bentley, 2014). A sediment accumulation rate was developed using following formulae:

$$S_{high} = (z_{high}) / (T\text{-}1963) \quad (5)$$

$$S_{deep} = (z_{deep}) / (T - 1954) \quad (6)$$

$$S_{avg} = (S_{high} + S_{deep})/ 2 \quad (7)$$

The variables are defined as $z_{high}$ the highest activity of $^{137}$Cs at the profile's peak, $z_{deep}$ is the maximum depth of $^{137}$Cs penetration, SAR is the sediment accumulation rate, and T is the year in which the sample was collected.

All samples were analyzed on Canberra LEGe 3825 or BEGe 3825 detectors calibrated for energy and efficiency using standard reference materials (US National Institute of Standards and Technology, and International Atomic Energy Agency), with samples from a single core being restricted to one detector. Sample self-absorption for $^{210}$Pb gamma emissions was determined using the transmission method (Cochran and Masqué 2003). Activities associated with the 295 and 352 keV peaks of $^{214}$Pb and the 609 keV peak of $^{214}$Bi were averaged to determine the amount of supported $^{210}$Pb. Supported $^{210}$Pb activity is subtracted from total $^{210}$Pb activity to determine excess $^{210}$Pb activity.

Sediment accumulation rate (SAR) for $^{210}$Pb were calculated using Sigmaplot© by least-squares regressions on radionuclide data based on Eq. 8 from Muhammad et al. (2008) adapted from:

$$A_z=A_0e^{(-\lambda z/SAR)} \quad (8)$$

where $A_z$ is activity at depth z (dpm/g), $A_0$ is activity extrapolated to the sediment surface (dpm/g), $\lambda$ is the decay constant of radionuclide of interest (year$^{-1}$), and SAR is the sediment accumulation

rate estimated for $^{210}Pb$. An average sediment accumulation rate was calculated based on the results of the $^{137}Cs$ and $^{210}Pb$ (Smith and Bentley, 2014).

### 2.4 Local Mass Accumulation Rates

By removing the water as well as organic material present in samples a dry mineral fraction, the dry mineral densities were determined for each sample. These were multiplied by the sediment accumulation rate to derive the mass accumulation rate for inorganic mineral in the following formula:

$$\textit{Mass Accumulation Rate (g cm}^{-2}\textit{ yr}^{-1}\textit{)} = \textit{Avg Sediment Accumulation Rate (cm yr}^{-1}\textit{)} * \textit{Dry Mineral Density (g cm}^{-3}\textit{ yr}^{-1}\textit{)} \quad (9)$$

### 2.5 Grain Size Analysis

A portion of the wet sample was for retained granulometry. Wet samples were prepared in a 0.05% sodium metaphosphate ($NaPO_3$) solution to assist in deflocculating sediment grains, and organic material was removed by manually sieving at 800 microns, and chemical digestion with 30% hydrogen peroxide. Grain size measurement was conducted in the Beckman-Coulter (LS-13-320SW) laser diffraction particle size analyzer. Mean, median, modal averages, along with percentages for clay, silt, and sand, for each sample were recorded and a frequency contour plot for each core was created.

### 2.6 Geographic Information System (GIS) Methodology and Regional Mass Accumulation Rates ($MAR_R$)

Using publicly available GIS data from the State of Louisiana ATLAS website (Louisiana ATLAS website, 2017), a total of 16 quadrangle maps containing LIDAR digital elevation models were obtained. These models were established with the vertical datum NAVD88 (GEOID99) in feet. The horizontal datum uses NAD 83, UTM Zone 15 N (WKID 26915) in meters. Horizontal resolution was five meters. Vertical resolution was two feet (converted to 0.61 meters). A grey-

scale model, based on the LIDAR elevation values, of the quadrangle map mosaic with an elevation range from 3 meters to 21 meters (Figure 7) illustrates the ridge and swale topographic relief of the study area. The total study area was measured at 270 $km^2$ using ArcGIS (Louisiana ATLAS website, 2017).

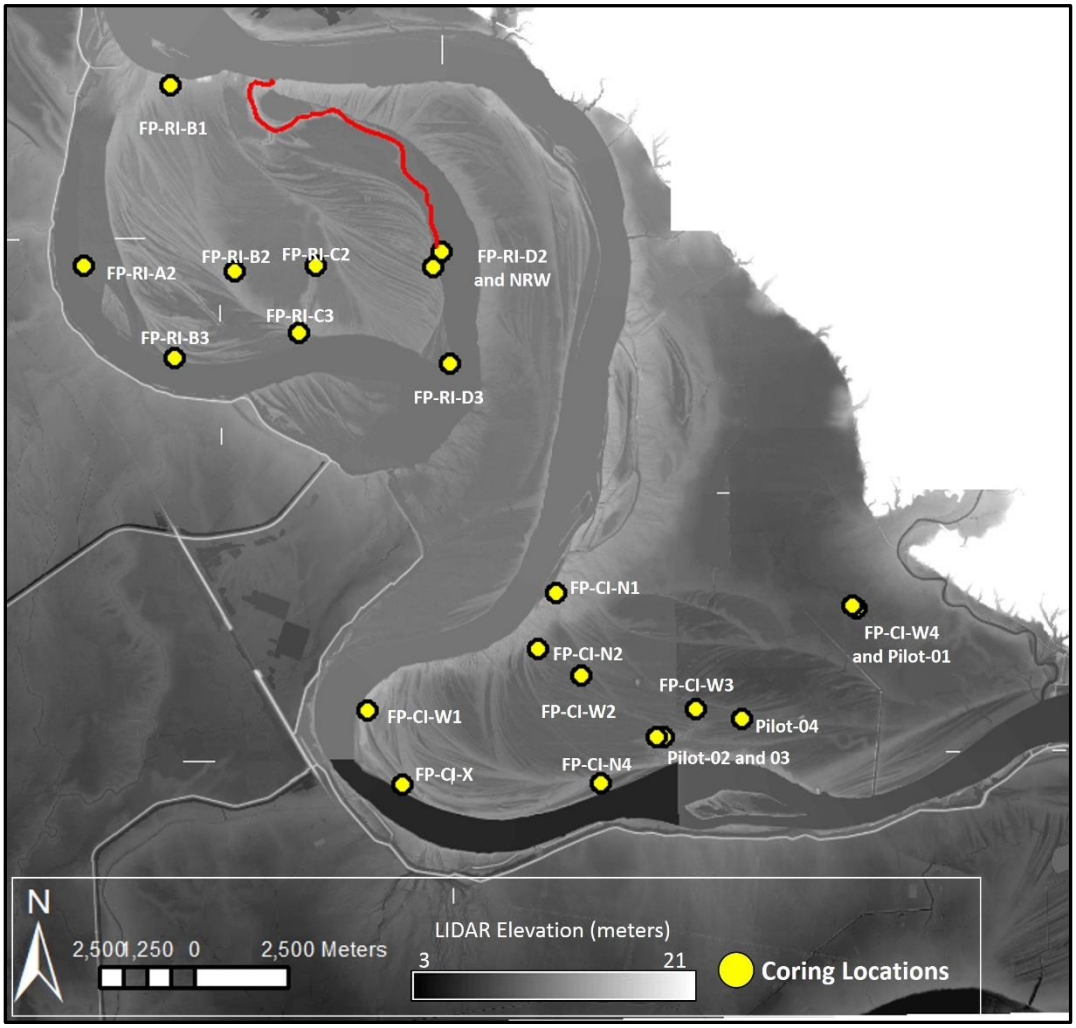


**Figure 7.** LIDAR Digital Elevation Model showing coring locations (Photo credit: State of Louisiana ATLAS website, accessed April 2017).

## 3. RESULTS

### 3.1 Radiochemistry and Geochronology

Sediment accumulation rates were determined for $^{210}$Pb and $^{137}$Cs. A total of five cores retained $^{137}$Cs activity to the base of the core, in which case the accumulation rates estimated are minimum values. The SARs for $^{137}$Cs ranged from 0.19 cm yr$^{-1}$ to greater than 1.10 cm yr$^{-1}$. The SARs for $^{210}$Pb ranged from 0.22 cm yr$^{-1}$ to greater than 1.3 cm yr$^{-1}$. Five cores showed no observable $^{210}$Pb activity or profiles that could not be fit using Equation 8, thus in these cores, the SAR was determined using only $^{137}$Cs. The average sediment accumulation rates range from 0.30 to to greater than 1.0 cm yr$^{-1}$. The average was determined by averaging the sediment accumulation rates from $^{137}$Cs and $^{210}$Pb. Sediment accumulation rates and mass accumulation rates from the 2014 pilot study (Smith and Bentley, 2014) have also been included with the results set.

**Table 4.** Cat Island (east bank) core radioisotope activity, sediment accumulation rates, and mass accumulation rates.

| Core Name | Maximum Activity Depth (cm) | $^{137}$Cs SAR (cm y$^{-1}$) | $^{210}$Pb SAR (cm y$^{-1}$) | Mean SAR (cm y$^{-1}$) |
|---|---|---|---|---|
| Pilot-01 | -- | 0.200 | 0.41 | 0.305 ± 0.11 |
| Pilot-02 | -- | 0.590 | 1.5 | 1.045 ± 0.46 |
| Pilot-03 | -- | 0.590 | 0.56 | 0.575 ± 0.02 |
| Pilot-04 | -- | 0.500 | 0.28 | 0.39 ± 0.11 |
| FP-CI-N1 | 66 | >1.10 ± 0.03 | -- | > 1.10 ± 0.03 |
| FP-CI-N2 | 24 | 0.376 ± 0.03 | 0.216 ± 0.05 | 0.296 ± 0.08 |
| FP-CI-N4 | 60 | 0.891 ± 0.03 | -- | 0.891 ± 0.03 |
| FP-CI-X | 46 | 0.692 ± 0.03 | 1.09 ± 1.86 | 0.891 ± 0.20 |
| FP-CI-W1 | 22 | 0.415 ± 0.04 | -- | 0.415 ± 0.03 |
| FP-CI-W2 | 40 | 0.630 ± 0.03 | 0.590 ± 0.32 | 0.61 ± 0.02 |
| FP-CI-W3 | 54 | 0.746 ± 0.03 | 0.638 ± 0.27 | 0.692 ± 0.05 |
| FP-CI-W4 | 14 | 0.226 ± 0.03 | -- | 0.226 ± 0.03 |

**Table 5.** Raccourci Island (west bank) core radioisotope activity, sediment accumulation rates, and mass accumulation rates.

| Core Name | Maximum Activity Depth (cm) | $^{137}$Cs SAR (cm y$^{-1}$) | $^{210}$Pb SAR (cm y$^{-1}$) | Mean SAR (cm y$^{-1}$) |
|---|---|---|---|---|
| FP-RI-A2 | > 28 | >0.190 ± 0.01 | > 0.243 ± 0.03 | > 0.217 ± 0.03 |
| FP-RI-B1 | > 60 | >0.968 ± 0.03 | -- | > 0.968 ± 0.03 |
| FP-RI-B2 | 70 | 0.984 ± 0.03 | 1.104 ± 0.51 | 1.044 ± 0.06 |
| FP-RI-B3 | 26 | 0.226 ± 0.02 | 0.630 ± 0.13 | 0.428 ± 0.20 |
| FP-RI-C2 | 30 | 0.413 ± 0.03 | 2.072 ± 0.96 | 0.908 ± .083 |
| FP-RI-C3 | 50 | 0.426 ± 0.02 | 0.767 ± 0.15 | 0.597 ± 0.17 |
| FP-RI-D2 | 52 | 0.558 ± 0.02 | 0.359 ± 0.04 | 0.458 ± 0.10 |
| FP-RI-D3 | > 20 | > 0.318 ± 0.03 | > 0.302 ± 0.07 | > 0.310 ± 0.01 |
| FP-RI-NRW | > 38 | > 0.571 ± 0.03 | > 0.941 ±0.33 | > 0.756 ± 0.18 |

### 3.2 Grain Size Analysis

The maximum grain size present in the samples was limited to 800 μm through sieving during sample preparation, to eliminate large organic particles that might harm the granulometric instrument. However, the maximum grain size presented in any core was less than 300 μm (medium-grained sand). A contour plot (Figures 10-26) for each core was created to illustrate the changes in grain size and frequency of the grains present.

**Table 6.** Cat Island (east bank) whole core granulometry percentages, median and modal grain size.

| Core Name | Clay Percentage | Silt Percentage | Sand Percentage | Core Median Grain Size (μm) | Core Modal ($d_{50}$) Grain Size (μm) |
|---|---|---|---|---|---|
| FP-CI-N1 | 13.36 | 28.57 | 58.07 | 88.6 | 127.4 |
| FP-CI-N2 | 56.17 | 42.34 | 1.49 | 8.3 | 15.9 |
| FP-CI-N4 | 54.29 | 43.86 | 1.84 | 8.7 | 19.0 |
| FP-CI-X | 46.76 | 50.04 | 3.20 | 11.7 | 27.1 |
| FP-CI-W1 | 30.71 | 56.68 | 12.60 | 26.1 | 41.2 |
| FP-CI-W2 | 34.84 | 56.71 | 8.44 | 20.0 | 38.0 |
| FP-CI-W3 | 52.27 | 45.66 | 2.06 | 10.3 | 17.0 |
| FP-CI-W4 | 73.86 | 24.97 | 1.18 | 5.3 | 10.7 |

**Table 7.** Raccourci Island (west bank) whole core granulometry percentages, median and modal grain size.

| Core Name | Clay Percentage | Silt Percentage | Sand Percentage | Core Median Grain Size (μm) | Core Modal ($d_{50}$) Grain Size (μm) |
|---|---|---|---|---|---|
| FP-RI-A2 | 73.38 | 25.63 | 0.98 | 5.2 | 6.1 |
| FP-RI-B1 | 19.26 | 41.99 | 38.75 | 61.6 | 102.4 |
| FP-RI-B2 | 49.78 | 48.88 | 1.28 | 8.0 | 15.8 |
| FP-RI-B3 | 10.17 | 32.62 | 57.21 | 70.7 | 87.9 |
| FP-RI-C2 | 19.95 | 59.73 | 20.32 | 29.3 | 46.4 |
| FP-RI-C3 | 21.27 | 51.30 | 27.43 | 25.9 | 47.3 |
| FP-RI-D2 | 9.47 | 27.12 | 63.40 | 45.9 | 67.0 |
| FP-RI-D3 | 14.07 | 35.93 | 50.00 | 33.2 | 45.9 |
| FP-RI-NRW | 25.56 | 50.19 | 24.25 | 29.7 | 47.9 |

### 3.3 Dry Mineral Density and Local Mass Accumulation Rates

A dry mineral density was calculated for each sample along the length of each core. The average dry mineral density for each core ranges from 0.335- 1.55 g $cm^{-3}$. An average dry mineral density of 1.07 g $cm^{-3}$ was determined for all cores in the study area; with an average for Cat Island (east bank) of 1.05 g $cm^{-3}$; and an average for Raccourci Island (west bank) of 1.08 g $cm^{-3}$. Based on the individual dry mineral density results for each core and the mean sediment accumulation rate for each core, mass accumulation rates were determined for each core (Tables 9 and 10). Mass accumulation rates range from 0.073 to greater than 1.48 g $cm^{-2}$ $y^{-1}$ (Figures 9 and 10).

**Table 8.** Cat Island (east bank) Average Dry Mineral Density and Mass Accumulation Rates. *Note: Mass accumulation rates for pilot cores sourced from Smith and Bentley, 2014. Dry mineral density for pilot cores calculated from SAR and MAR data.

| Core Name | Average Mineral Mass Fraction | Calculated Dry Mineral Density (g $cm^{-3}$) | Mean SAR (cm $y^{-1}$) | Mass Accumulation Rate (MAR) (g $cm^{-2}$ $y^{-1}$) |
|---|---|---|---|---|
| Pilot-01* | N/A | 1.02 | 0.305 ± 0.11 | 0.31 |
| Pilot-02* | N/A | 1.06 | 1.045 ± 0.46 | 1.11 |
| Pilot-03* | N/A | 1.06 | 0.575 ± 0.02 | 0.61 |
| Pilot-04* | N/A | 1.05 | 0.390 ± 0.11 | 0.41 |
| FP-CI-N1 | 0.981 | 1.35 | > 1.098 ± 0.03 | > 1.48 |
| FP-CI-N2 | 0.934 | 0.781 | 0.296 ± 0.08 | 0.231 |
| FP-CI-N4 | 0.949 | 1.16 | 0.891 ± 0.03 | 1.04 |
| FP-CI-X | 0.938 | 1.13 | 0.891 ± 0.20 | 1.006 |
| FP-CI-W1 | 0.939 | 1.22 | 0.415 ± 0.04 | 0.505 |
| FP-CI-W2 | 0.959 | 0.955 | 0.610 ± 0.02 | 0.582 |
| FP-CI-W3 | 0.948 | 0.892 | 0.692 ± 0.05 | 0.617 |
| FP-CI-W4 | 0.937 | 0.913 | 0.226 ± 0.03 | 0.206 |

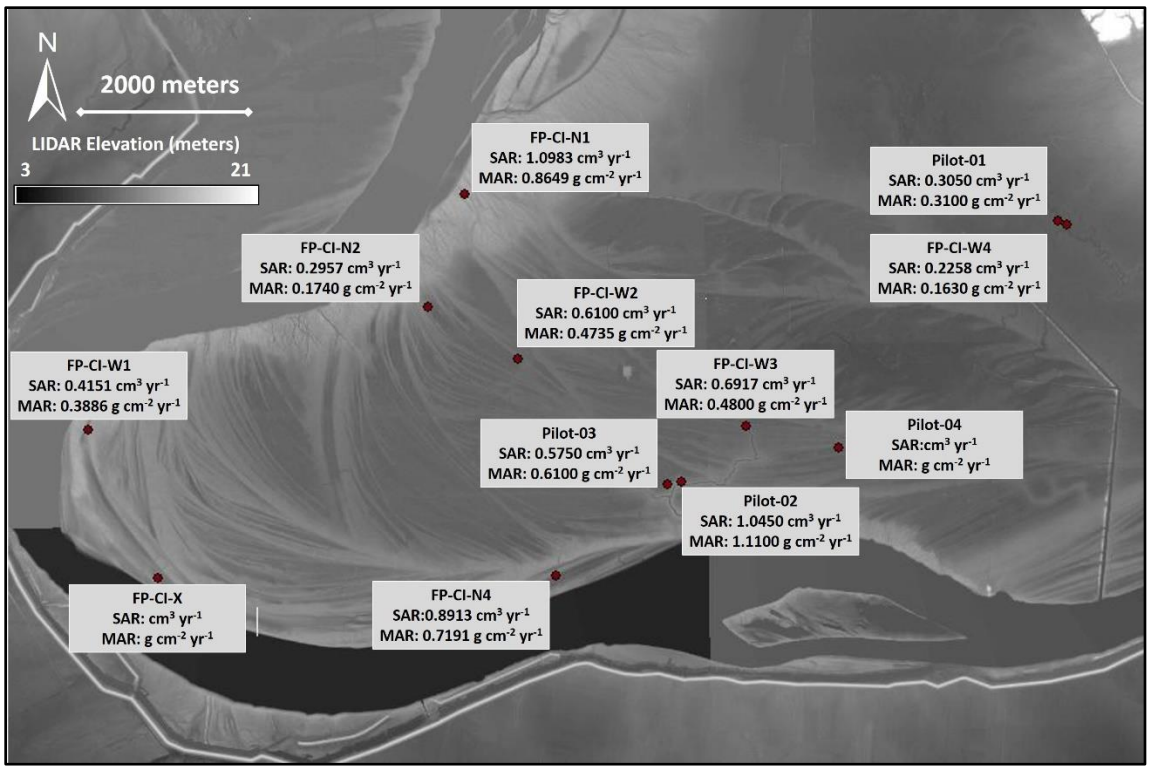


**Figure 8.** Cat Island (east bank) core locations illustrating SARs and MARs.

**Table 9.** Raccourci Island (west bank) Average Dry Mineral Density and Mass Accumulation Rates.

| Core Name | Average Mineral Mass Fraction | Calculated Dry Mineral Density (g $cm^{-3}$) | Mean SAR (cm $y^{-1}$) | Mass Accumulation Rate (MAR) (g $cm^{-2}$ $y^{-1}$) |
|---|---|---|---|---|
| FP-RI-A2 | 0.933 | 0.335 | > 0.217 ± 0.03 | 0.073 |
| FP-RI-B1 | 0.981 | 1.36 | > 0.968 ± 0.03 | 1.31 |
| FP-RI-B2 | 0.944 | 1.23 | 1.044 ± 0.06 | 1.29 |
| FP-RI-B3 | 0.972 | 1.29 | 0.428 ± 0.20 | 0.552 |
| FP-RI-C2 | 0.945 | 0.927 | 0.908 ± 0.08 | 0.841 |
| FP-RI-C3 | 0.988 | 1.55 | 0.597 ± 0.17 | 0.927 |
| FP-RI-D2 | 0.946 | 1.24 | 0.458 ± 0.10 | 0.569 |
| FP-RI-D3 | 0.936 | 0.825 | > 0.310 ± 0.01 | 0.255 |
| FP-RI-NRW | 0.976 | 0.984 | > 0.756 ± 0.18 | 0.744 |

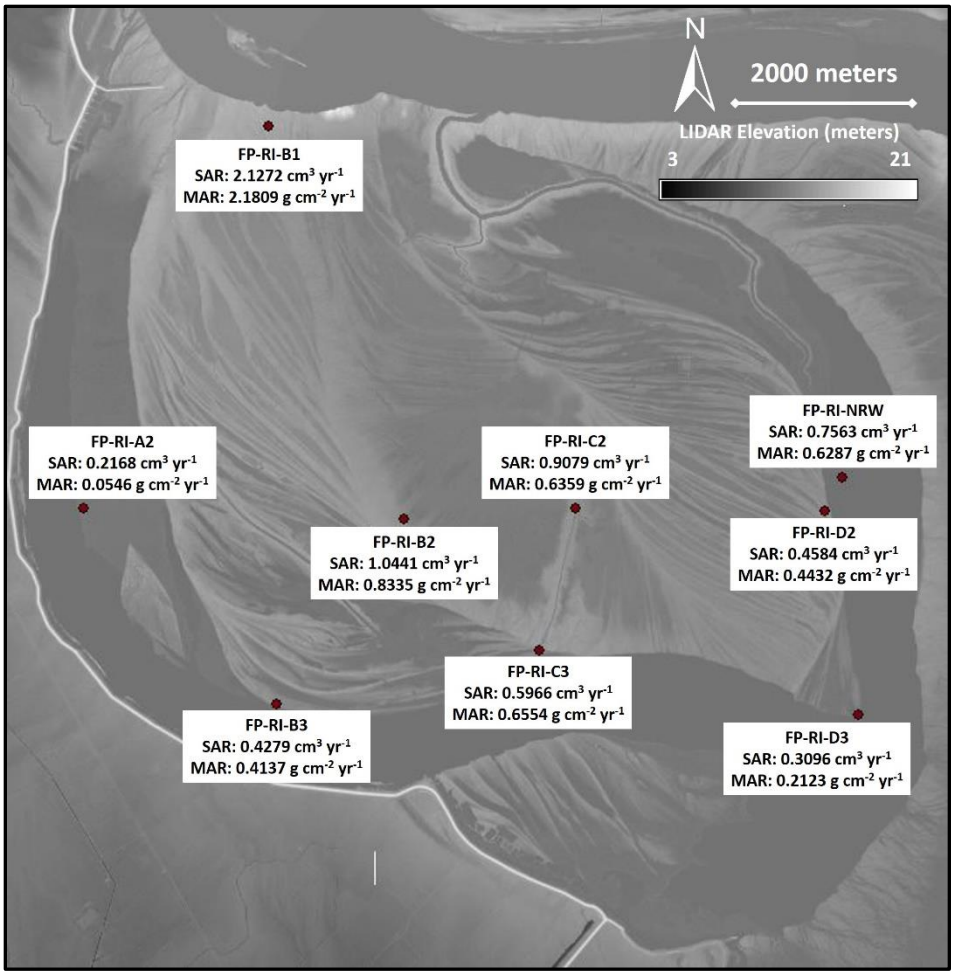


**Figure 9.** Raccourci Island core locations illustrating sediment accumulation rates and mass accumulation rates.

Figures 10-26 illustrate the radiochemical and granulometry data. Figures on the left illustrate radiochemical changes through the core. The figures on the right illustrate the granulometric changes. Grain size is represented as a color-contoured frequency plot with vertical lines illustrating clay-silt and silt-sand boundaries (3.9 and 62.5 microns, respectively).

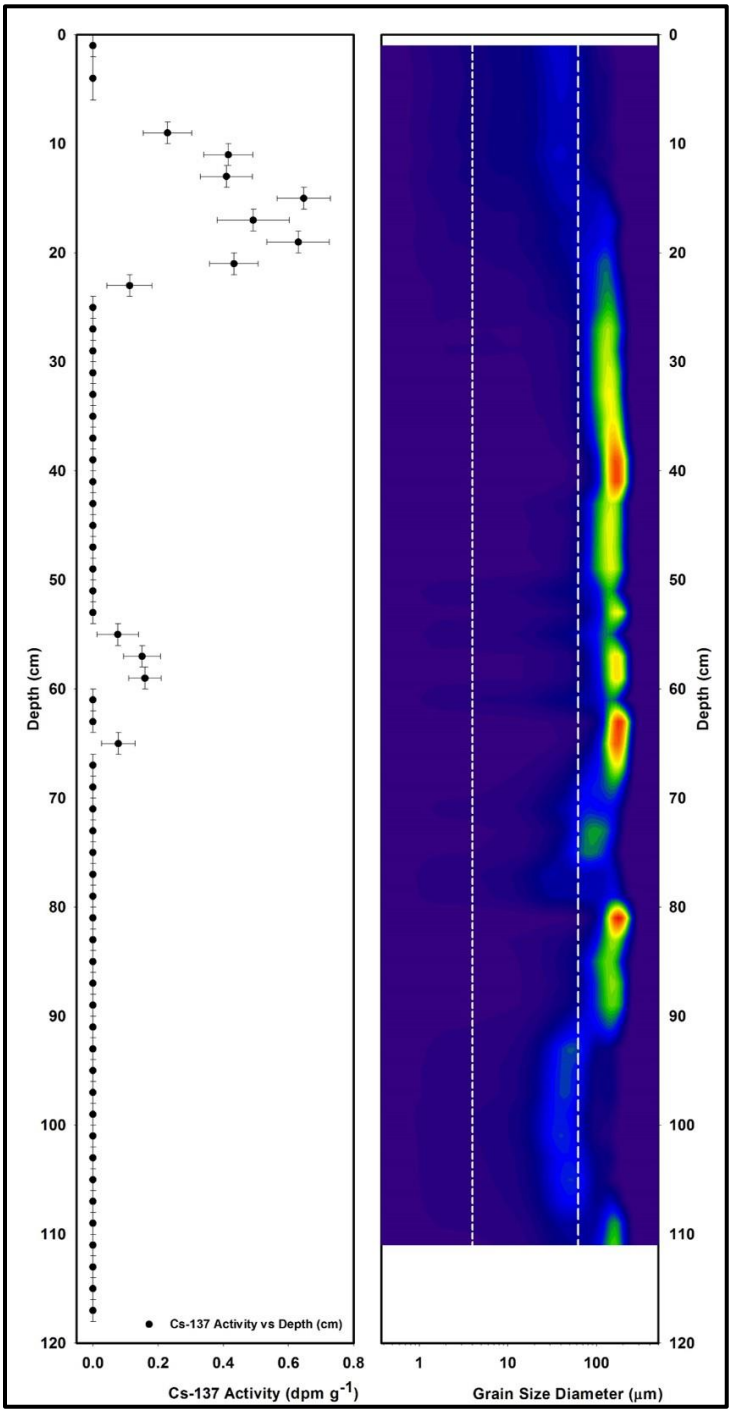

**Figure 10.** Core FP-CI-N1. SAR > 1.098 ± 0.03 cm $yr^{-1}$, MAR > 1.48 g $cm^{-2}$ $yr^{-1}$. Core consists primarily of very fine sands.

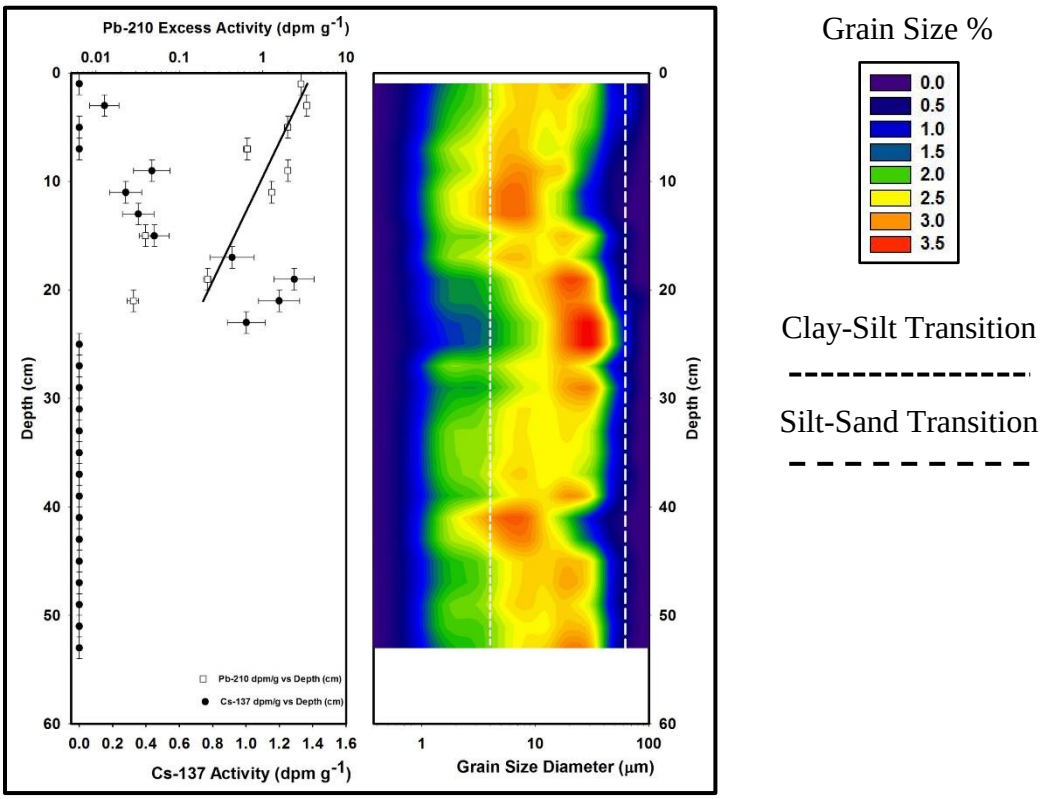


**Figure 11.** Core FP-CI-N2. SAR = 0.296 ± 0.08 cm $yr^{-1}$; MAR = 0.231 g $cm^{-2}$ $yr^{-1}$. Core consists primarily of clays and silt.

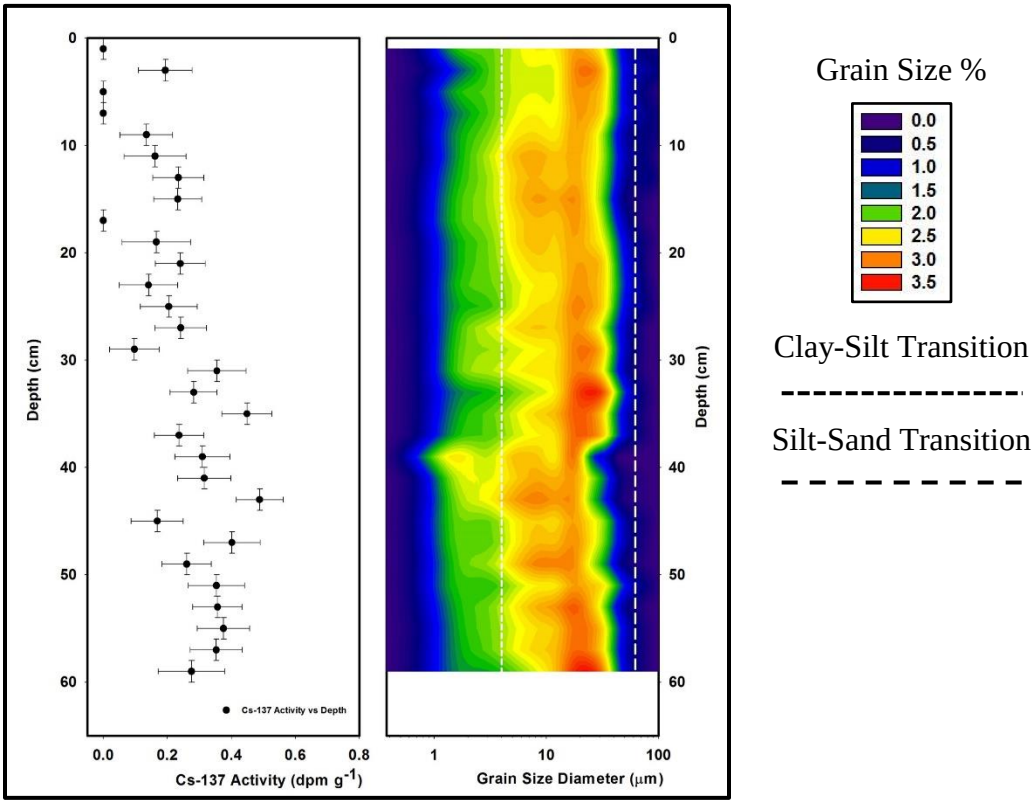


**Figure 12.** Core FP-CI-N4. SAR = 0.891 ± 0.03 cm $yr^{-1}$; MAR = 1.037 g $cm^{-2}$ $yr^{-1}$. Core consists primarily of clays and silt.

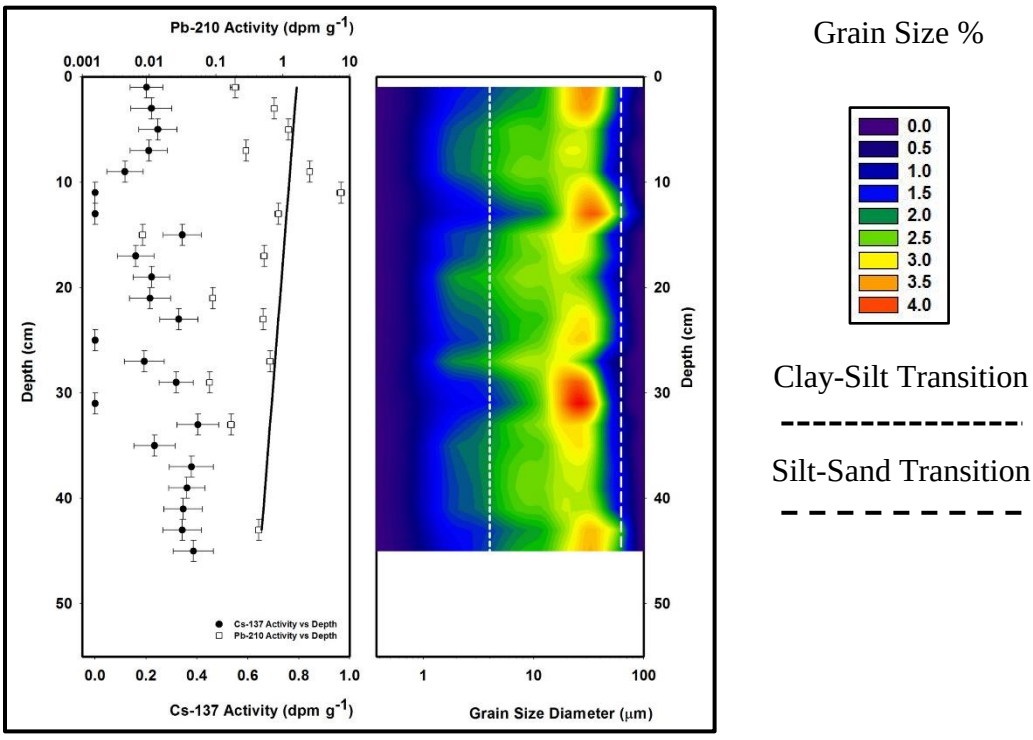

**Figure 13.** Core FP-CI-X. SAR = 0.891 ± 0.2 cm $yr^{-1}$; MAR = 1.006 g $cm^{-2}$ $yr^{-1}$. Core consists primarily of silt with some clay.

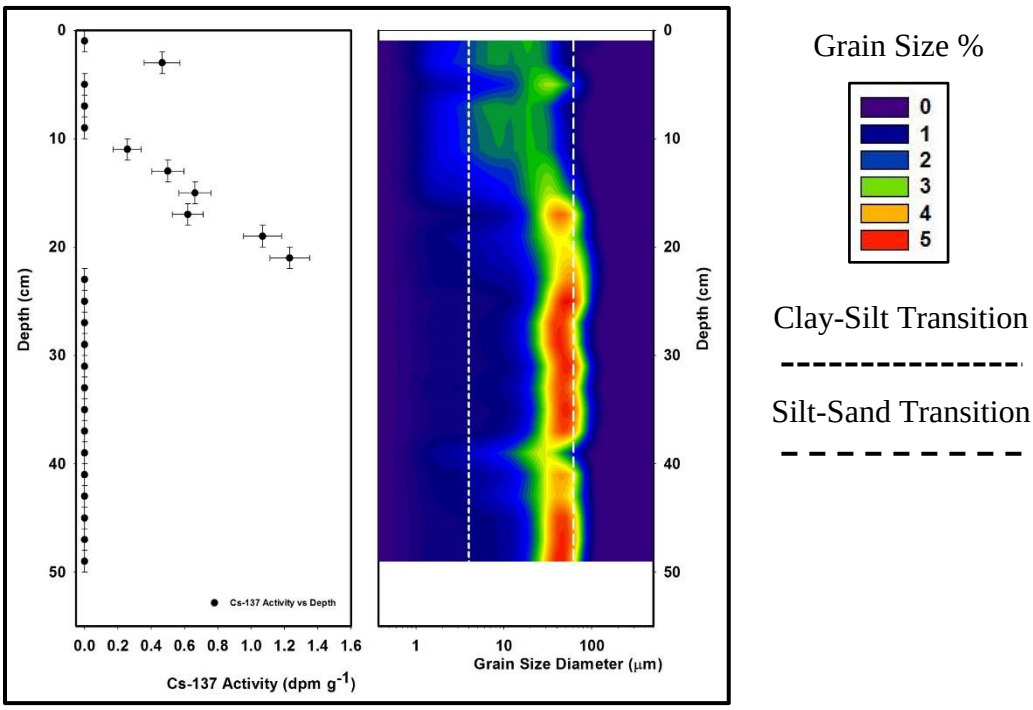


**Figure 14.** Core FP-CI-W1.SAR = 0.415 ± 0.04 cm $yr^{-1}$; MAR = 0.505 g $cm^{-2}$ $yr^{-1}$. Core consists primarily of silt.

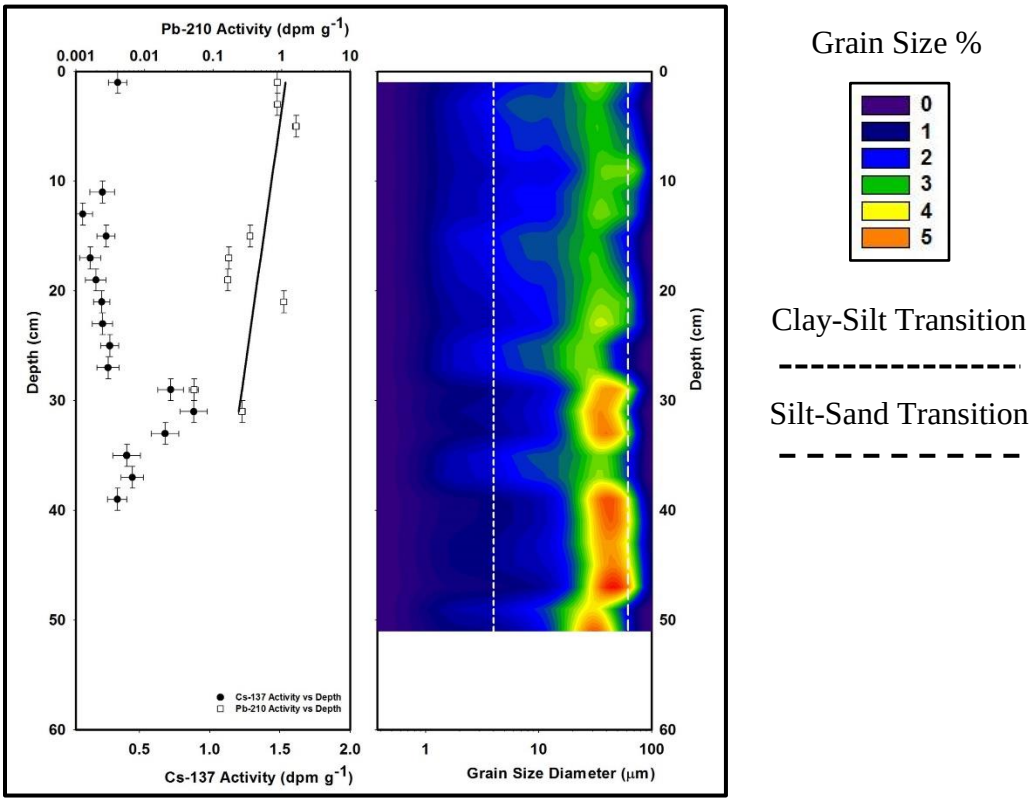


**Figure 15.** Core FP-CI-W2. SAR = 0.61 ± 0.02 cm $yr^{-1}$; MAR = 0.582 g $cm^{-2}$ $yr^{-1}$.Core consists primarily of silt.

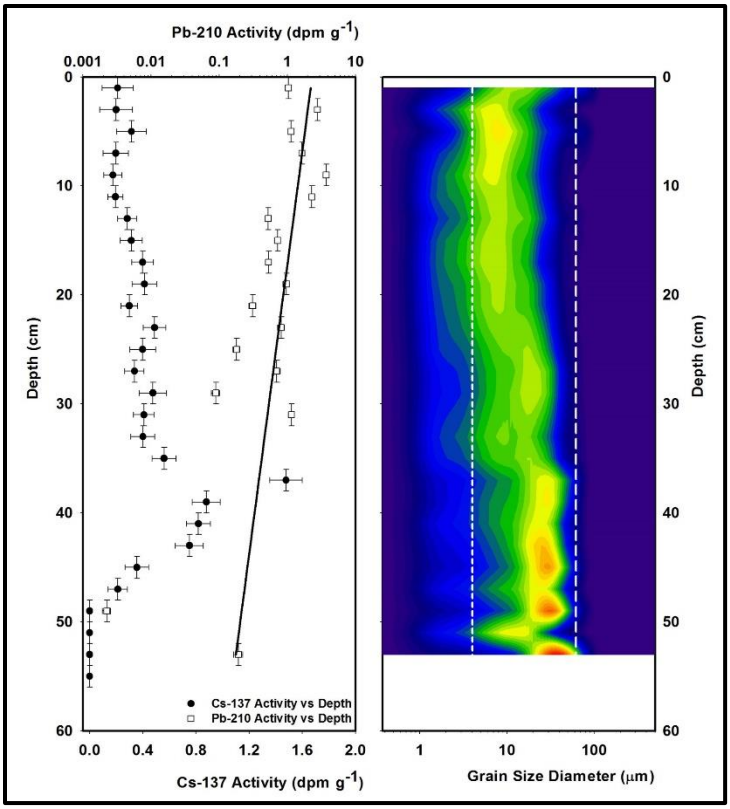


**Figure 16.** Core FP-CI-W3. SAR = 0.692 ± 0.05 cm $yr^{-1}$; MAR = 0.617 g $cm^{-2}$ $yr^{-1}$. Core consists primarily of silt and clay.

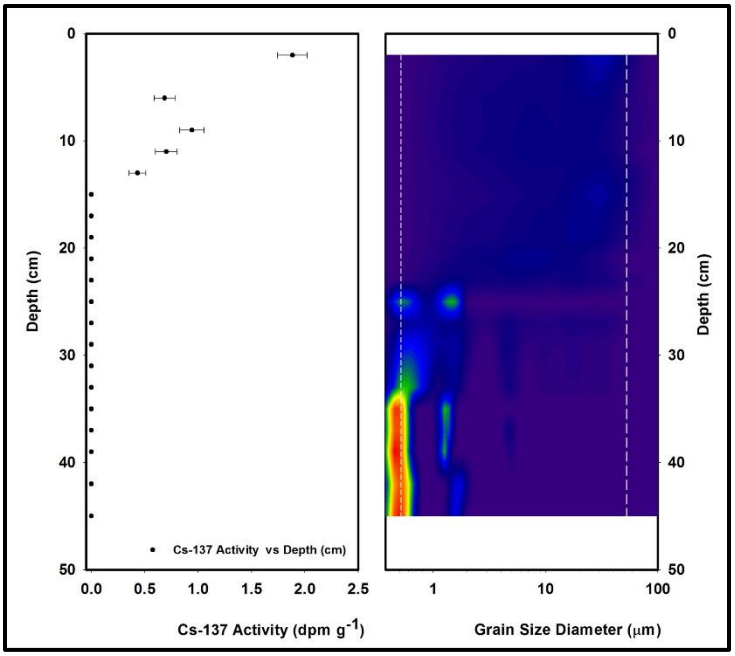


**Figure 17.** Core FP-CI-W4. SAR = 0.226 ± 0.03 cm $yr^{-1}$; MAR = 0.206 g $cm^{-2}$ $yr^{-1}$. Core consists primarily of clay.

On Cat Island, the cores exhibiting the coarsest material, including coarse-grained silt to fine-grained sand, were found nearest the main channel of the Mississippi River. Additionally, the cores with coarser material had exhibited the highest dry mineral densities. When sediment accumulation rates were greater than 0.7 cm $yr^{-1}$, the dry mineral densities were also greater than 1 gm $cm^{-3}$. Lower sediment accumulation rates exhibited dry mineral densities less than 1.0 g $cm^{-3}$.

These grain size and dry mineral density trends had a significant impact on the calculations used to determine the mass accumulation rates. The combined effect of increased sediment accumulation rate and increased dry mineral density enhanced the resulting mass accumulation rates and led to more pronounced differences in mass accumulation rate. The result is that the highest mass accumulation rates were found near the main channel of the Mississippi River along the natural levee.

The cores take from Racccourci Island are presented in groups of three. The subaqueous cores and Core FP-RI-D2 (Figures 18-20) have been grouped together. The cores taken furthest inland, FP-RI-B2 and FP-RI-C2 with core FP-RI-B1 (Figures 21-23) have been grouped together. And the cores of the southern edge of Raccourci Island, FP-RI-B3, FP-RI-C3, and FP-RI-D3 (Figures 24-26) have been grouped together.

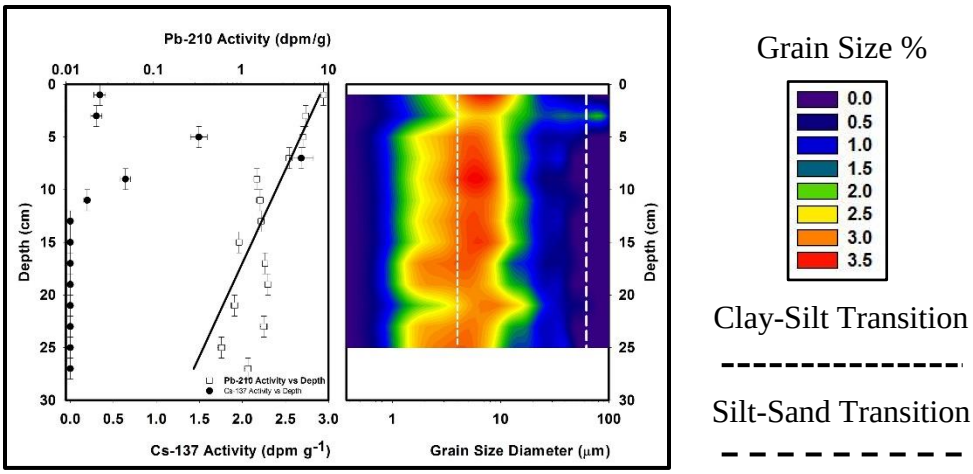


**Figure 18.** Core FP-RI-A2. SAR > 0.217 ± 0.03 cm $yr^{-1}$; MAR = 0.073g $cm^{-2}$ $yr^{-1}$. Core consists primarily of clay. Contained the highest amounts of organic content.

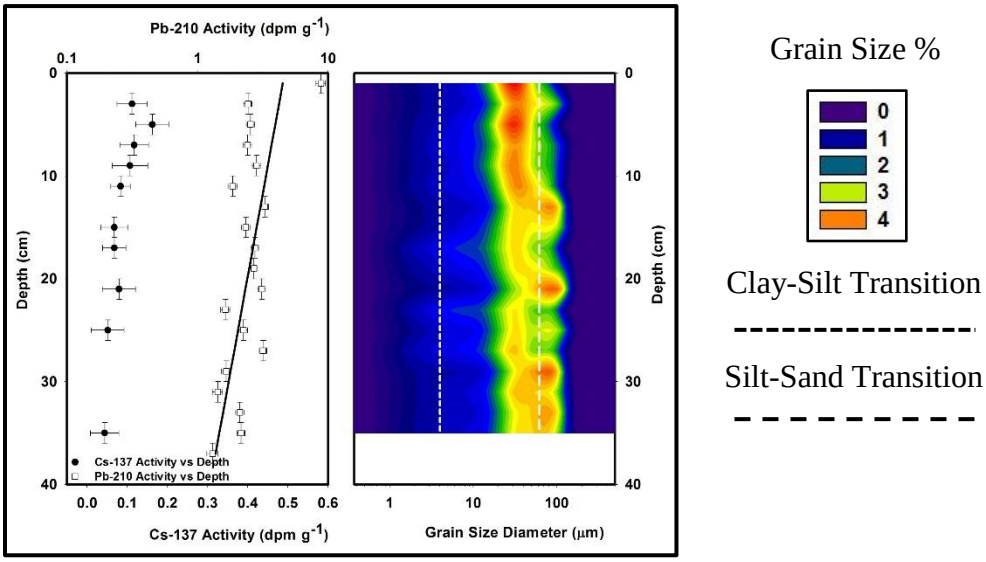


**Figure 19.** Core FP-RI-NRW. SAR > 0.756 ± 0.18 cm $yr^{-1}$; MAR = 0.744 g $cm^{-2}$ $yr^{-1}$. Core consists primarily of silt.

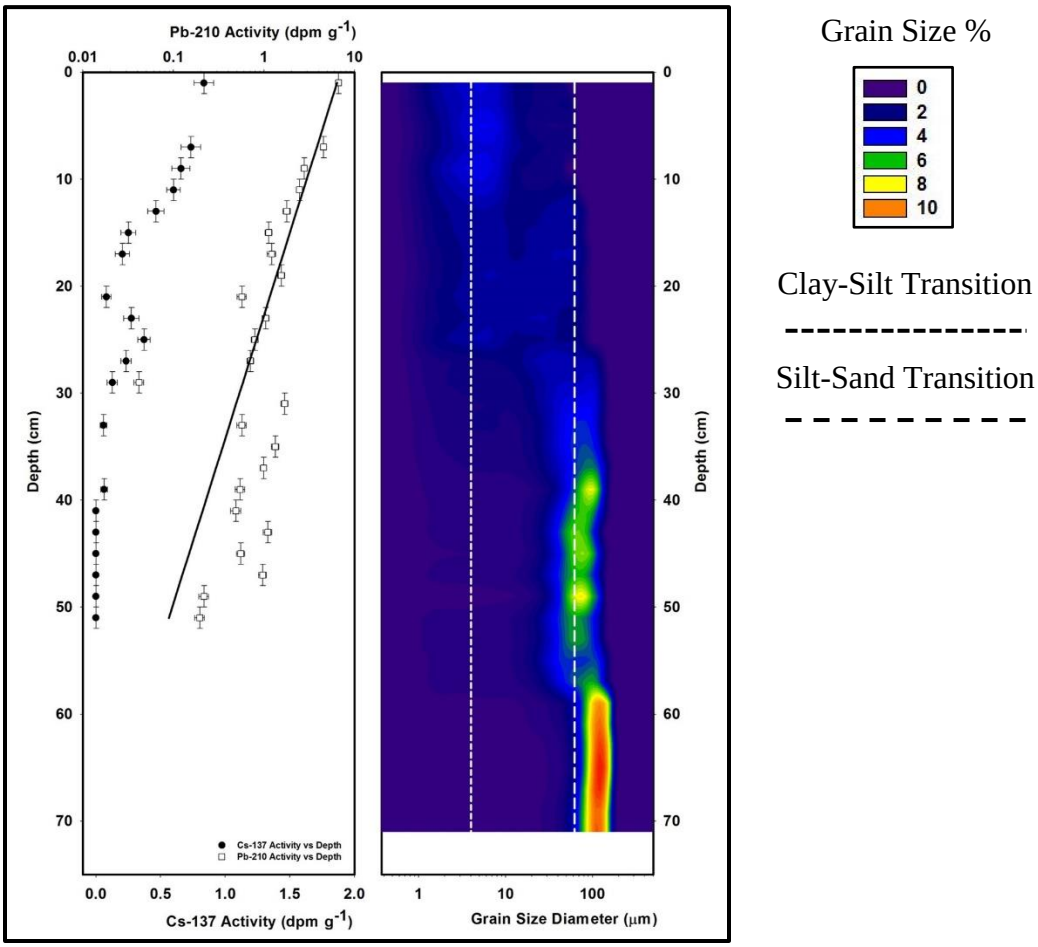


**Figure 20.** Core FP-RI-D2. SAR = 0.458 ± 0.10 cm $yr^{-1}$ MAR = 0.569 g $cm^{-2}$ $yr^{-1}$. Core consists primarily of very fine sand.

The subaqueous cores exhibited very different characteristics from each other in spite of their similar environment. Core FP-RI-A2 was taken furthest from the tie channel and was located in a forested area containing organic material in higher proportion than all other cores. Due to this increased organic material, the dry mineral density was greatly reduced. With a low sedimentation rate (0.217 g $cm^{-2}$ $yr^{-1}$) and the reduced dry mineral density, the resulting mass accumulation rate was the lowest of all cores. Conversely, Core FP-RI-NRW was taken from the subaqueous lacustrine delta. It had a sediment accumulation rate (0.756 g $cm^{-2}$ $yr^{-1}$) near the average of the cores taken from Raccourci Island with a dry mineral density just below 1 g $cm^{-3}$, leading to a

mass accumulation rate of 0.744 g $cm^{-2}$ $yr^{-1}$. Core FP-RI-D2 was near the lacustrine delta and exhibited a sediment accumulation rate below 0.5 cm $yr^{-1}$, but had a high dry mineral density, leading to an increased mass accumulation rate of 0.569 g $cm^{-2}$ $yr^{-1}$.

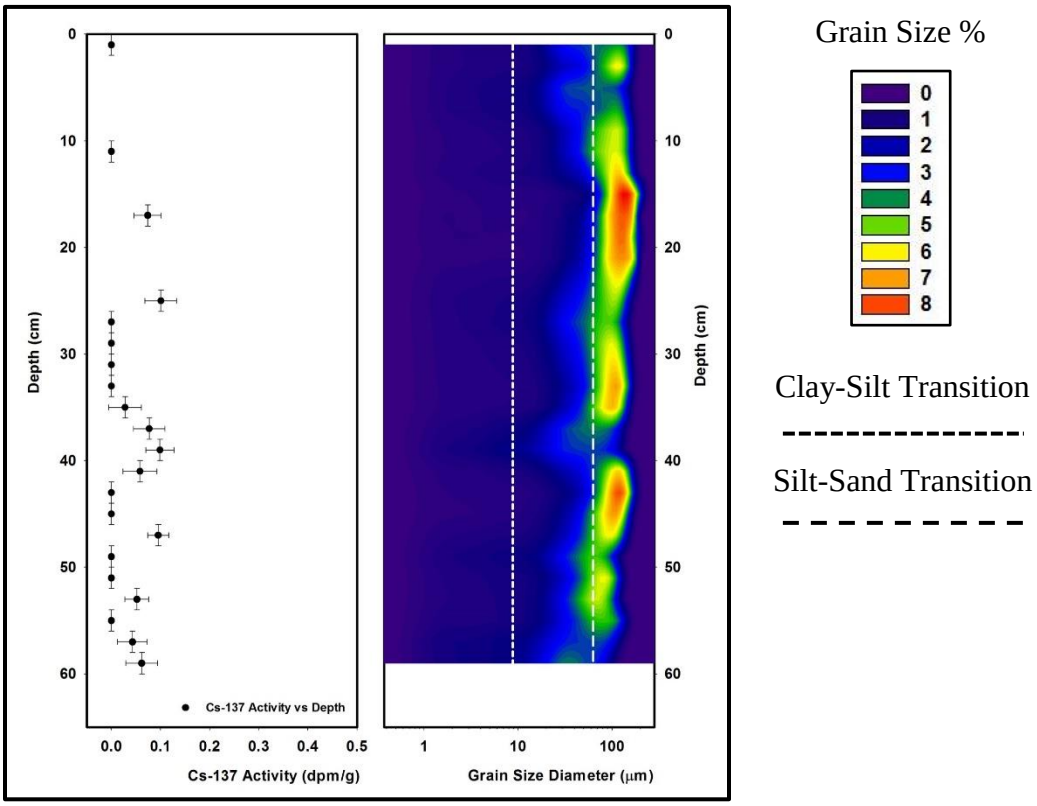


**Figure 21.** Core FP-RI-B1. SAR > 0.968 ± 0.03 cm $yr^{-1}$; MAR > 1.31 g $cm^{-2}$ $yr^{-1}$. Core consists primarily of very fine sand with silt.

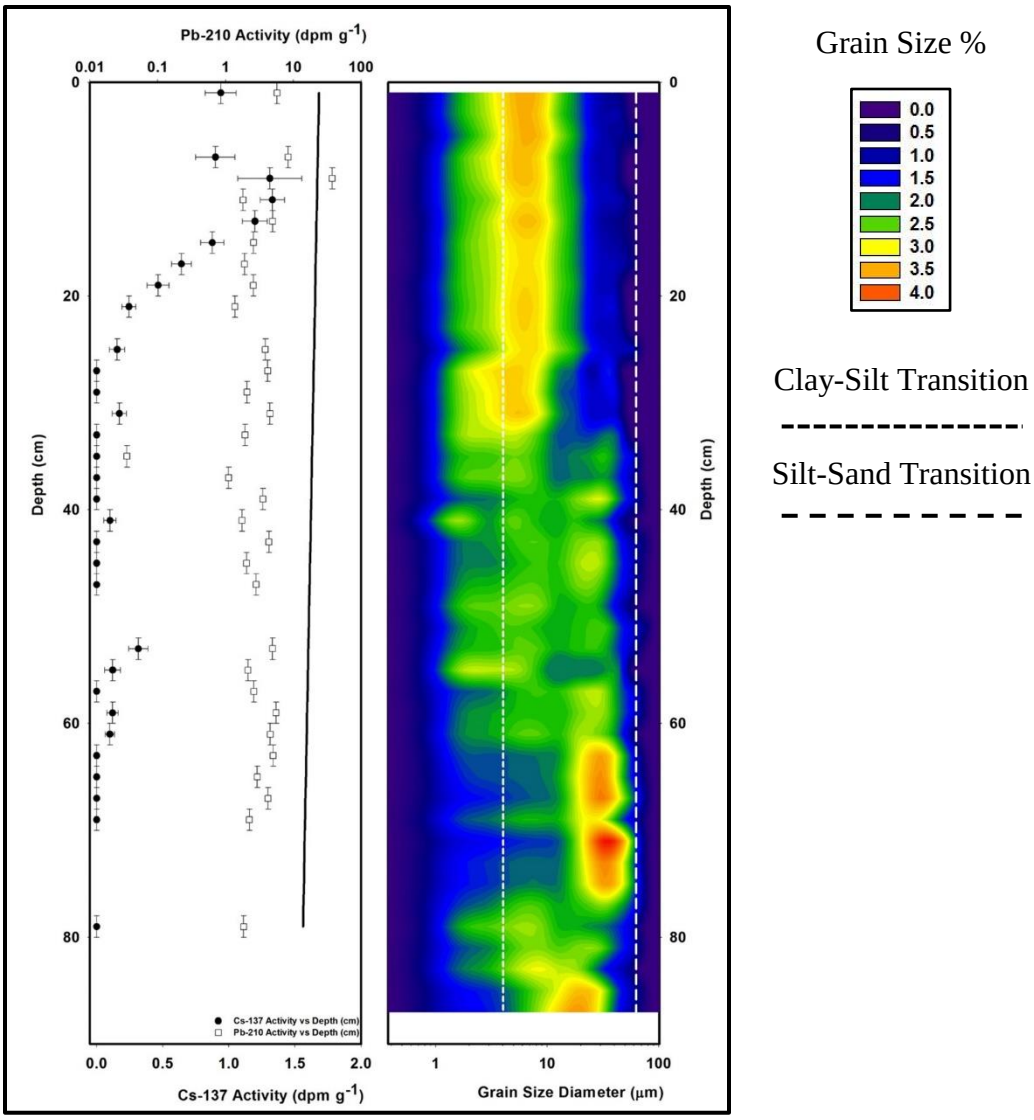


**Figure 22.** Core FP-RI-B2. SAR = 1.044 ±0.06 cm $yr^{-1}$; MAR = 1.29 g $cm^{-2}$ $yr^{-1}$. Core contains a significant portion of clay at the top with increasing silt at the bottom.

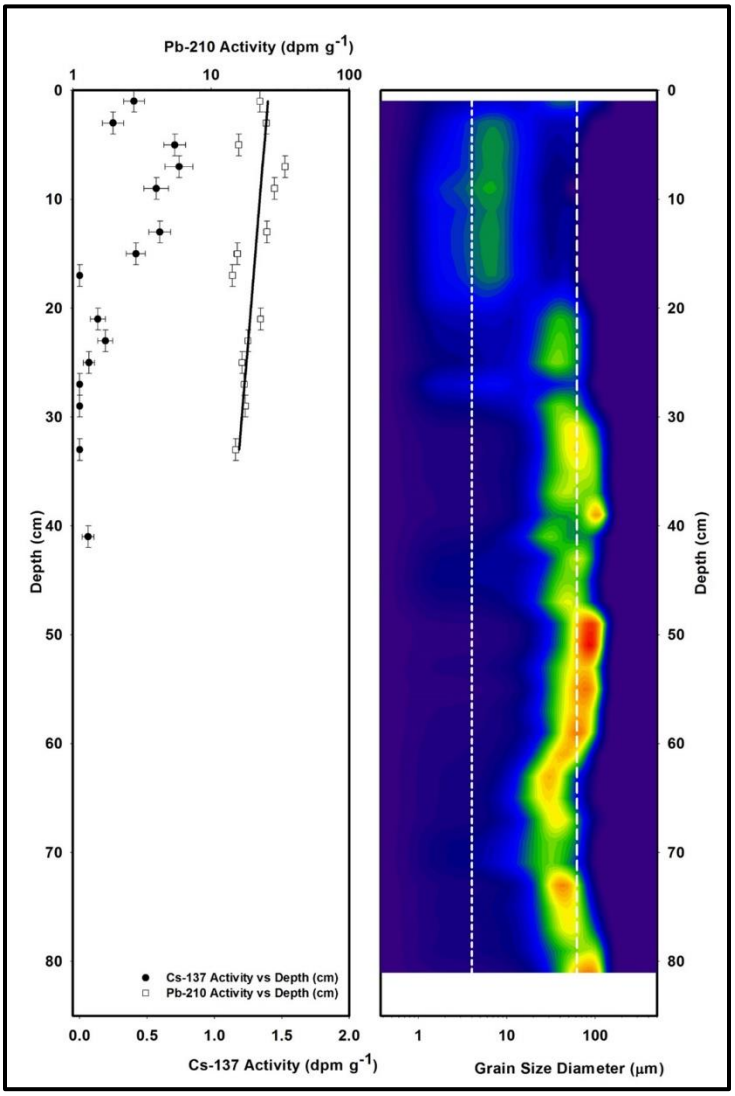


**Figure 23.** Core FP-RI-C2. SAR = 0.908 ± 0.83 cm $yr^{-1}$; MAR = 0.841 g $cm^{-2}$ $yr^{-1}$. Core consists primarily of silt and very fine sand.

The three cores above, FP-RI-B1, FP-RI-B2, and FP-RI-C2 each exhibited the highest sedimentation rates and dry mineral densities greater than 0.9 g $cm^{-3}$. When reviewing the LIDAR imagery, each of the above cores appears to be located near the apex of separate scroll bars. These cores also exhibited higher content of coarser material including very fine to fine-grained sand.

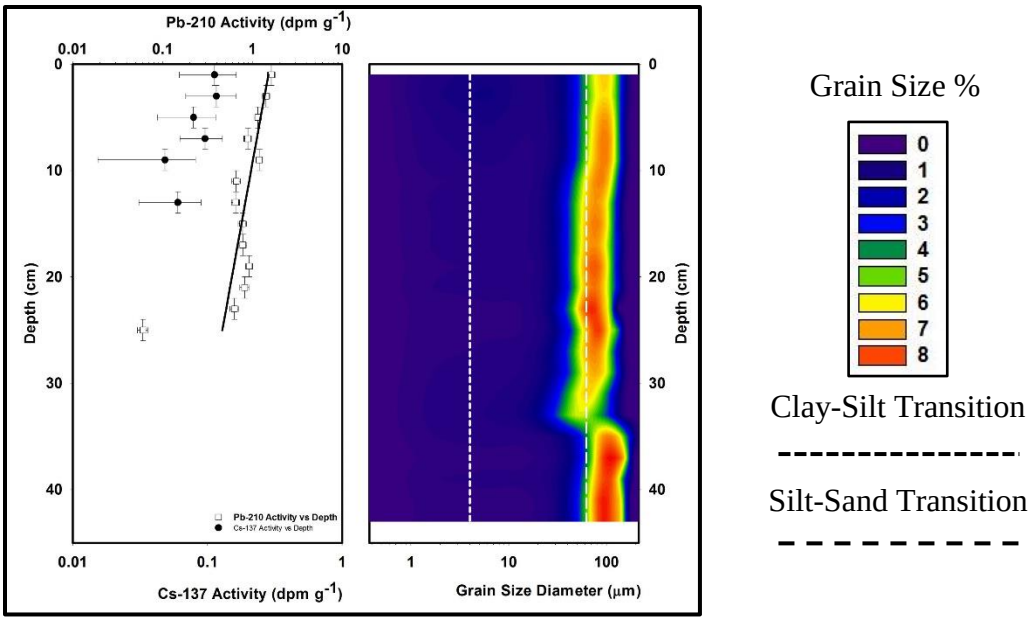


**Figure 24.** Core FP-RI-B3. SAR = 0.428 ± 0.2 cm $yr^{-1}$; MAR = 0.552 ± 0.19 g $cm^{-2}$ $yr^{-1}$. Core consists primarily of fine-grained sands.

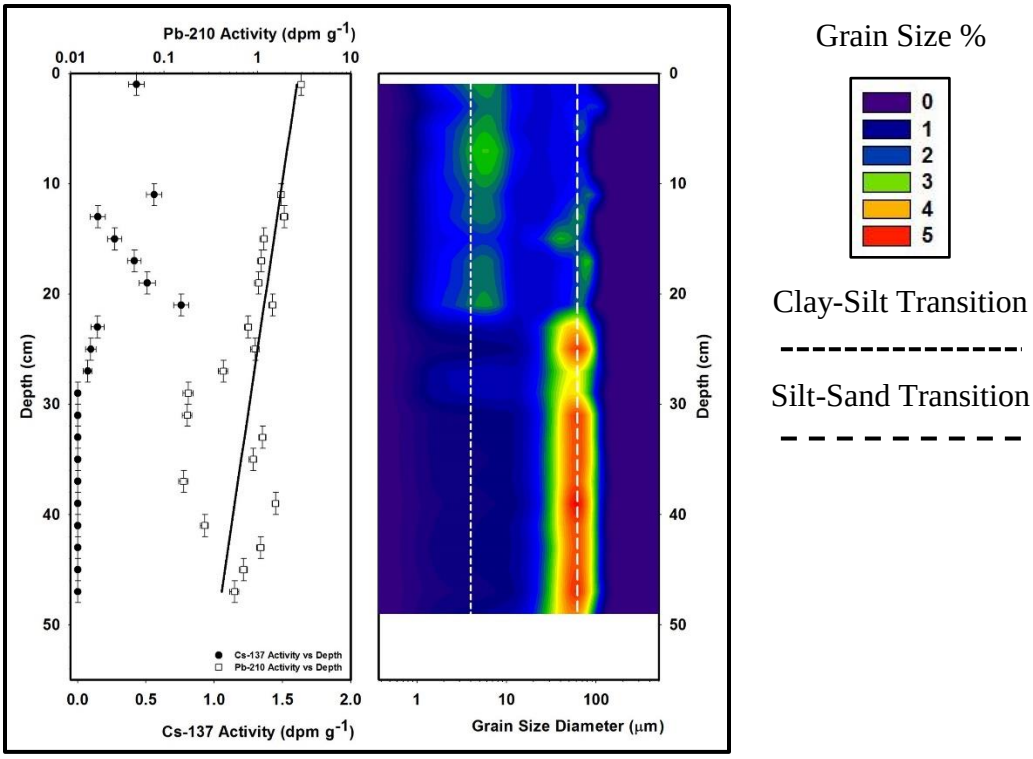


**Figure 25.** Core FP-RI-C3. SAR = 0.597 ± 0.17 cm $yr^{-1}$; MAR = 0.927 ± 0.19 g $cm^{-2}$ $yr^{-1}$. Core consists primarily of clay in the upper portion and silt to fine-grained sands below 23 cm.

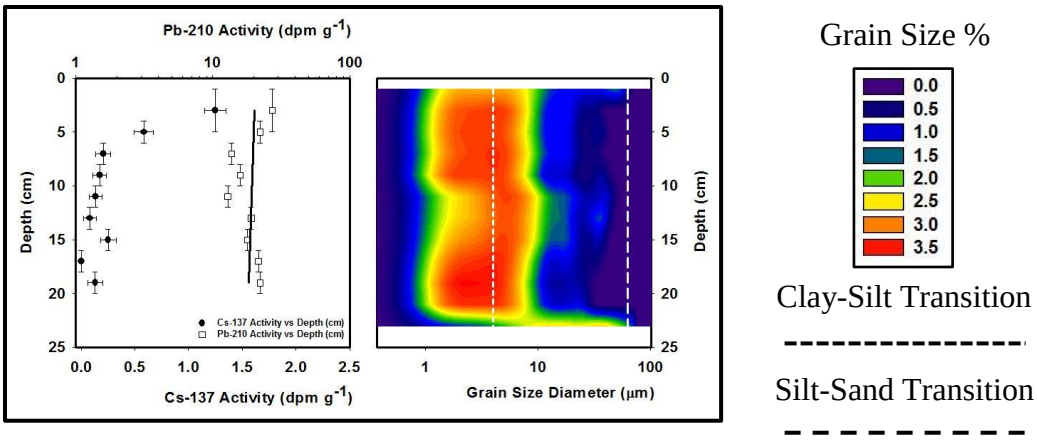


**Figure 26.** Core FP-RI-D3. SAR > 0.31 ± 0.01 cm $yr^{-1}$; MAR > 0.255 ± 0.01 g $cm^{-2}$ $yr^{-1}$. Core consists primarily of silt and significant amounts of clay. At the bottom of the core, a transition to silt and sand begins.

The cores located along the southern edge of Raccourci Island near the banks of Raccourci Old River also exhibited higher levels of the coarse-grained silt and fine-grained sand. However, these cores all had decreased sediment accumulation rates compared to the cores near the apex of a scroll bar, at the lacustrine delta, or near the active Mississippi River main channel. A possible explanation for the decreased sedimentation rates is that the distance from active deposition to southern edge of Raccourci Island is too far to support higher rates of sedimentation. Cores FP-CI-B3 and FP-CI-C3 exhibited higher dry mineral densities than Core FP-RI-D3, resulting in higher mass accumulation rates compared to FP-RI-D3.

# 4. DISCUSSION

## 4.1 Granulometry Effects on Radiochemical Signatures and Sediment Density

Clay to medium-grained silt were the dominant sediment types in cores taken furthest inland. Very fine to fine grained-sand were the dominant sediment type observed in cores closest to the main channel of the Mississippi River or Raccourci Old River. Sandy cores tended to have lower activities of $^{210}$Pb and $^{137}$Cs; in cases where grain size effects introduced strong variability in $^{210}$Pb profiles, the regression approach could not be used for estimating SAR. However, $^{137}$Cs SARs were developed for all cores.

Based on the calculated dry mineral density and the calculated mass accumulation rate, a relationship between sediment accumulation rate and mass accumulation rate was established. The relationship between dry mineral density and mass accumulation rate was first investigated in order to establish the relationship between SARs and MARs. Analysis of dry mineral density vs. MAR resulted in an $r^2$ value of 0.46 (Figure 27); and analysis of SAR vs. MAR resulted in an $r^2$ value of 0.91 (Figure 28). The low density values expressed as dry mineral density are reflective of the removal of water and organic matter while keeping the volume of the original sample constant. While this is not reflective of the true sediment density, it was an effective means for converting the SAR value to the MAR value.

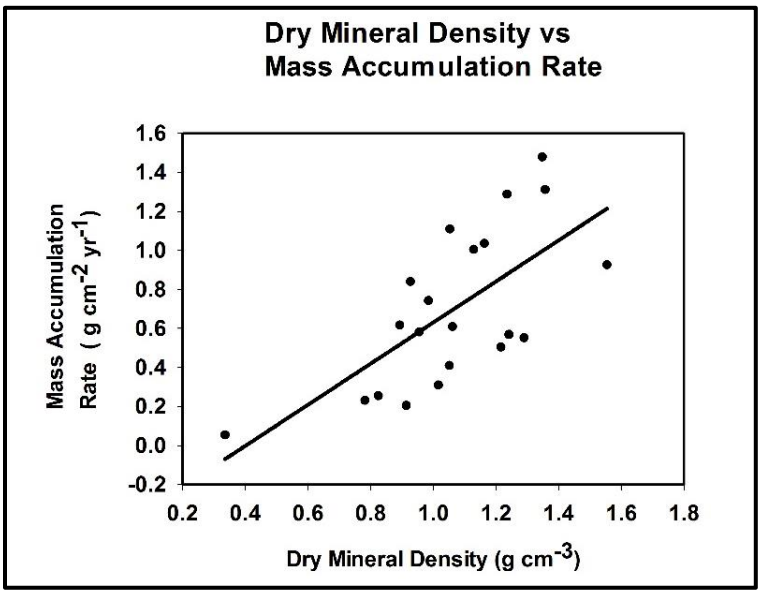


**Figure 27.** Dry mineral density relationship with mass accumulation rate (slope = 1.05 cm $yr^{-1}$; $r^2$ = 0.46)

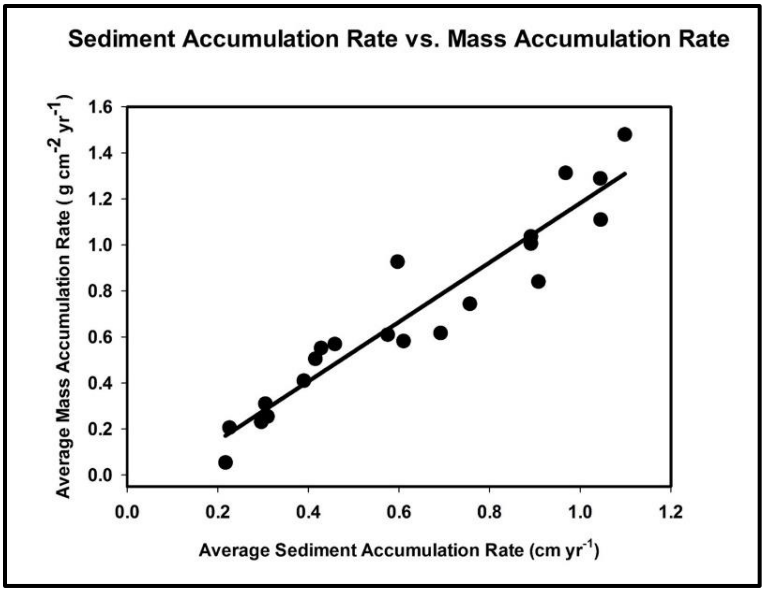


**Figure 28.** Linear relationship between sediment accumulation rate and converted mass accumulation rate (slope = 1.295 g $cm^{-3;}$ $r^2$ = 0.91).

### 4.2 Determining a Regional Mass Accumulation Rate ($MAR_R$)

After exploring the spatial distributions of MAR data (see below), regional mass accumulation rates ($MAR_R$) were determined using two methods. First, a natural neighbor interpolation for all 12 cores taken from Cat Island and for all nine cores taken from Raccourci

Island was applied to each study area to avoid crossing the Mississippi River main channel. This method only covered approximately one-third of the entire 270 $km^2$ study area and could not account explicitly for all geographic and topographic variations in the study area.

The second method used to determine $MAR_R$ was application of regression analyses based on two controlling spatial factors that appeared to account for the most spatial variability, from our initial analysis. The first spatial factor was distance from open water and the resultant change in MAR. The second spatial factor was elevation and the resultant change in MAR. This second method attempts to account for all geographic and topographic variations in the study area.

### 4.3 Regional Mass Accumulation Rates ($MAR_R$) – Natural Neighbor Interpolation

Using ArcMap, natural neighbor interpolation was conducted on each point bar within a polygon bounding the sampling locations. The resulting polygons for Cat Island and Raccourci Island covered 42.6 $km^2$ and 45.2 $km^2$ respectively (Figure 29). This interpolation method serves as a simple model of deposition that takes into account the entire sample population. While the topography within each polygon is broadly similar to the topography of the entire study area, the natural-neighbor polygons cover less than one-third of the total study area. The weighted average from each point bar was first applied for the area covered by the interpolation, and this result was then extrapolated to the larger polygons enclosing the full study area. The resulting mass accumulation rate based on this interpolation for the entire study area is 2.11 MT $yr^{-1}$ (Table 11).

**Table 10.** Regional Mass Accumulation Rates along the Mississippi River floodplain based natural neighbor interpolation.

| Storage Sink | Weighted Avg. Mass Accumulation Rate (g $cm^{-2}$ $yr^{-1}$) | Mass Accumulation Rate (MT $yr^{-1}$) | Displayed Polygon Area ($km^2$) | Extrapolated Mass Accumulation Rate (MT $yr^{-1}$) | Full Storage Sink Area ($km^2$) |
|---|---|---|---|---|---|
| Cat Island | 0.74 | 0.32 | 42.6 | 1.08 | 144 |
| Raccourci Island | 0.82 | 0.37 | 45.2 | 1.03 | 126 |
| Total | 0.156 | 0.69 | 87.8 | 2.11 | 270 |

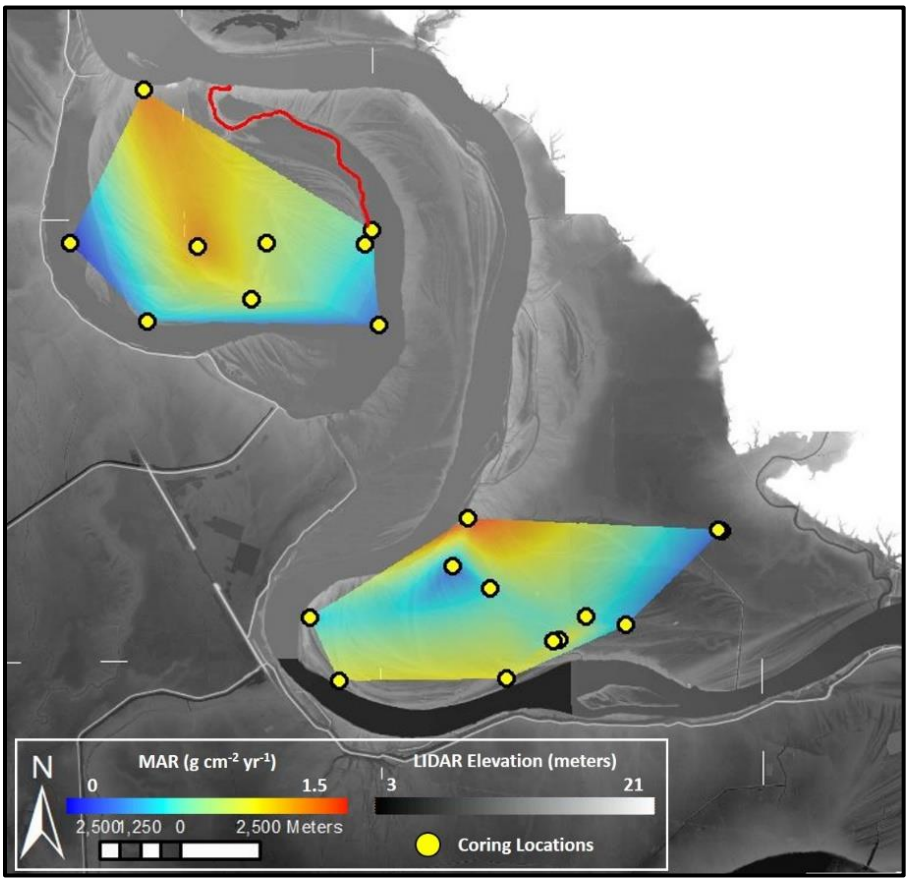


**Figure 29.** Expected mass accumulation rates throughout the study area based on natural neighbor interpolation. Results are included in Table 11.

### 4.4 Spatial Factors Affecting Mass Accumulation Rates

On a regional scale, an overall mass accumulation was investigated on the following two factors: distance from the Mississippi River or Raccourci Old River and elevation. A linear regression was tested in order to create a mass accumulation rate that changed with distance or with elevation using the following formulae:

$$\textit{Change based on Channel Distance} = (MAR - MAR_0) \div \textit{Channel Distance (meters)} \quad (10)$$

$$\textit{Change based on Elevation} = (MAR - MAR_0) \div \textit{Elevation (meters)} \quad (11)$$

As shown in Figure 30, the changing rate of deposition was better explained by elevation than by distance from the channel. However, low values of $r^2$ in each plot show that neither parameter accounts for the majority of variability in the entire population of cores. The distance and elevation regressions were then applied to the individual point bars.

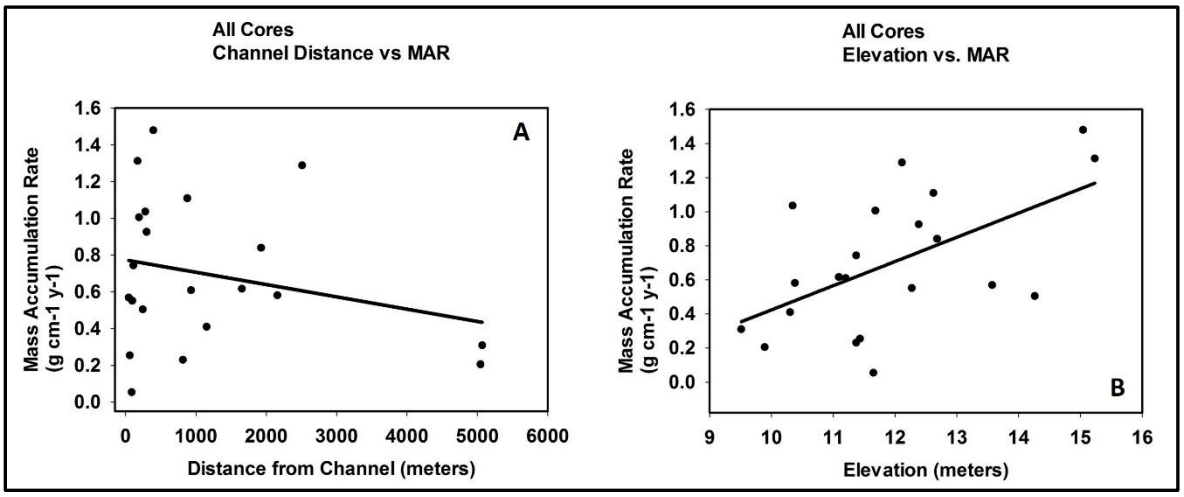


**Figure 30.** Analysis of the mass accumulation rates of all cores. Based on distance (a) shows that MARs changed by -6.69 x $10^{-5}$ g $cm^{-2}$ $y^{-1}$ for every meter of distance away from the river or oxbow lake ($r^2$ = 0.06). Based on elevation (b), MARs changed by 0.142 g $cm^{-2}$ $y^{-1}$ ($r^2$ = 0.32) for every meter of elevation gained.

**Table 11.** Cat Island (east bank) elevations, channel distances, and mass accumulation rates.

| Core Name | Distance from Channel (m) | Elevation (m) | MAR (g $cm^{-2}$ $y^{-1}$) |
|---|---|---|---|
| Pilot-01 | 5068 | 9.51 | 0.31 |
| Pilot-02 | 877 | 12.62 | 1.11 |
| Pilot-03 | 931 | 11.2 | 0.61 |
| Pilot-04 | 1150 | 10.3 | 0.41 |
| FP-CI-N1 | 440 | 15.21 | > 1.48 |
| FP-CI-N2 | 814 | 11.37 | 0.231 |
| FP-CI-N4 | 280 | 10.34 | 1.037 |
| FP-CI-X | 189 | 11.68 | 1.006 |
| FP-CI-W1 | 243 | 14.26 | 0.505 |
| FP-CI-W2 | 2156 | 10.38 | 0.582 |
| FP-CI-W3 | 1650 | 11.09 | 0.617 |
| FP-CI-W4 | 5044 | 9.89 | 0.206 |

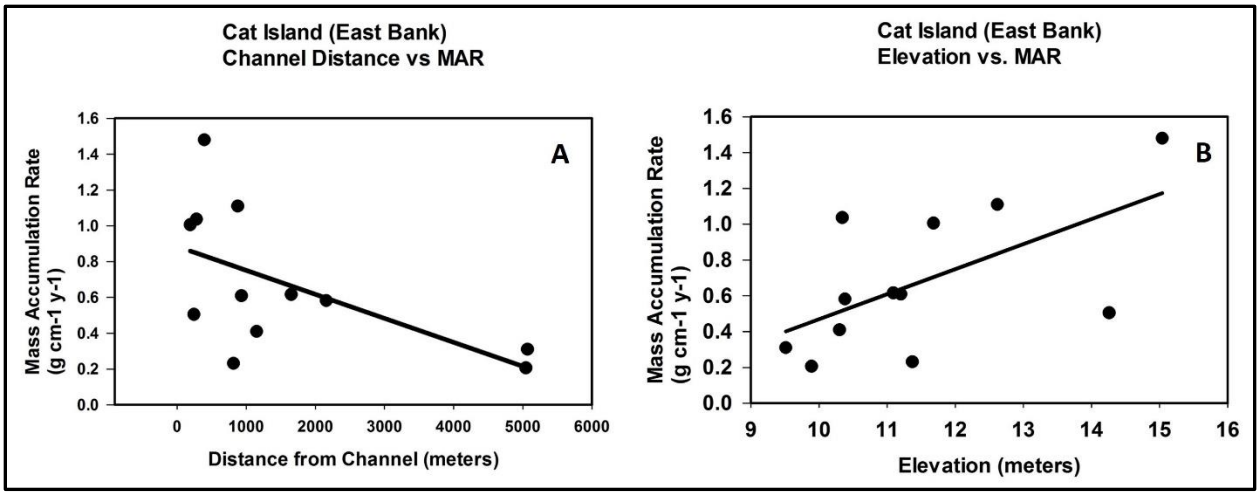


**Figure 31.** Analysis of the mass accumulation rates of cores taken from the east bank (Cat Island). Based on distance (a), MARs changed by -1.34 x $10^{-4}$ g $cm^{-2}$ $y^{-1}$ for every meter of distance away from the river or oxbow lake ($r^2$ = 0.34). Based on elevation (b), MARs changed by 0.139 g $cm^{-2}$ $y^{-1}$ ($r^2$ = 0.36) for every meter of elevation gained.

**Table 12.** Raccourci Island (west bank) elevations, channel distances, and mass accumulation rates.

| Core Name | Distance from Channel (m) | Elevation (m) | MAR (g $cm^{-2}$ $y^{-1}$) |
|---|---|---|---|
| FP-RI-A2 | 0 | 11.65 | 0.073 |
| FP-RI-B1 | 905 | 15.23 | 1.31 |
| FP-RI-B2 | 2506 | 12.11 | 1.29 |
| FP-RI-B3 | 83 | 12.27 | 0.552 |
| FP-RI-C2 | 1924 | 12.68 | 0.841 |
| FP-RI-C3 | 313 | 12.38 | 0.927 |
| FP-RI-D2 | 47 | 13.57 | 0.569 |
| FP-RI-D3 | 59 | 11.43 | 0.255 |
| FP-RI-NRW | 0 | 11.43 | 0.744 |

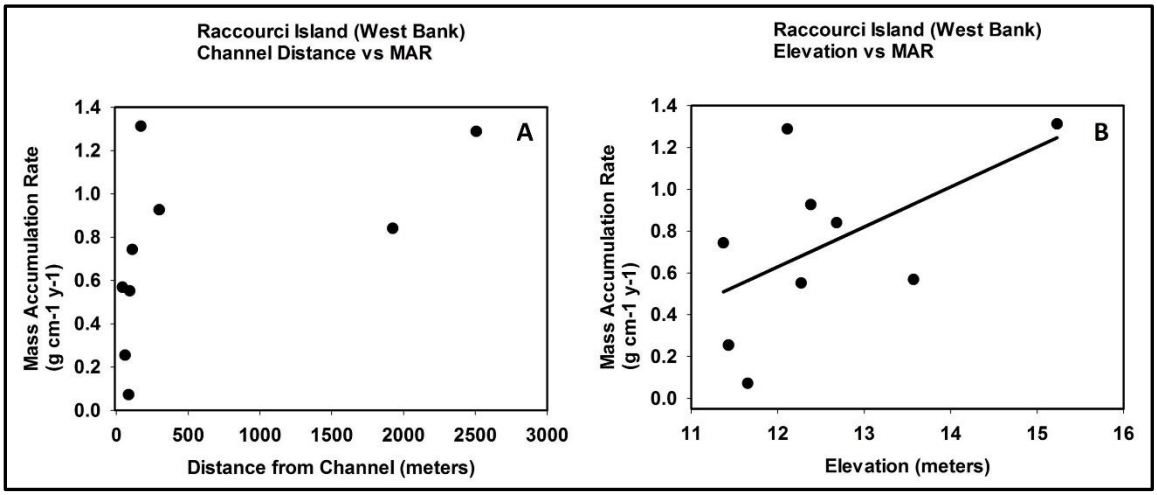


**Figure 32.** Analysis of the mass accumulation rates of cores taken from Raccourci Island (west bank). Based on distance (a), MARs changed by 3.061 x $10^{-4}$ g $cm^{-2}$ $y^{-1}$ for every meter of distance away from the river or oxbow lake ($r^2$ = 0.45). Based on elevation (b), MARs changed by 0.191 g $cm^{-2}$ $y^{-1}$ ($r^2$ = 0.31) for every meter of elevation gained.

This regression approach yielded values of $r^2$ <0.5, so data were further subdivided to identify spatial relationships that could explain more of the observed variability. In the next approach, data were first separated by overall location (Cat Island or Raccourci Island), then separated into groups of cores located 500 meters or closer to the river channel or lake shore, and greater than 500 meters from river channel or lake shore. Linear regressions were then calculated for the four data groups, regressing distance versus MAR for cores within 500 meters of open water, and elevation versus MAR for cores greater than 500 meters from open water.

A 500-meter buffer around Raccourci Old River and the main channel of the Mississippi River was created (Figure 33). Within the 500-meter zone, the formula for distance was applied to create a regression for these portions of the study area (Figure 34). The regression was then applied in ArcGIS to produce mass accumulation rate point values for each 5-meter by 5-meter pixel. The mass accumulation rate point value was expressed on an area of only 1 $cm^2$, therefore the rate was multiplied over the entire 25 $m^2$ area of each pixel to produce a total mass. All resulting point values were then summed to produce the total mass accumulation for each zone. Outside the 500-

meter zone, in the inland portions of each point bar, the formula for elevation was applied. A similar regression was created and then mass accumulation formula is applied.

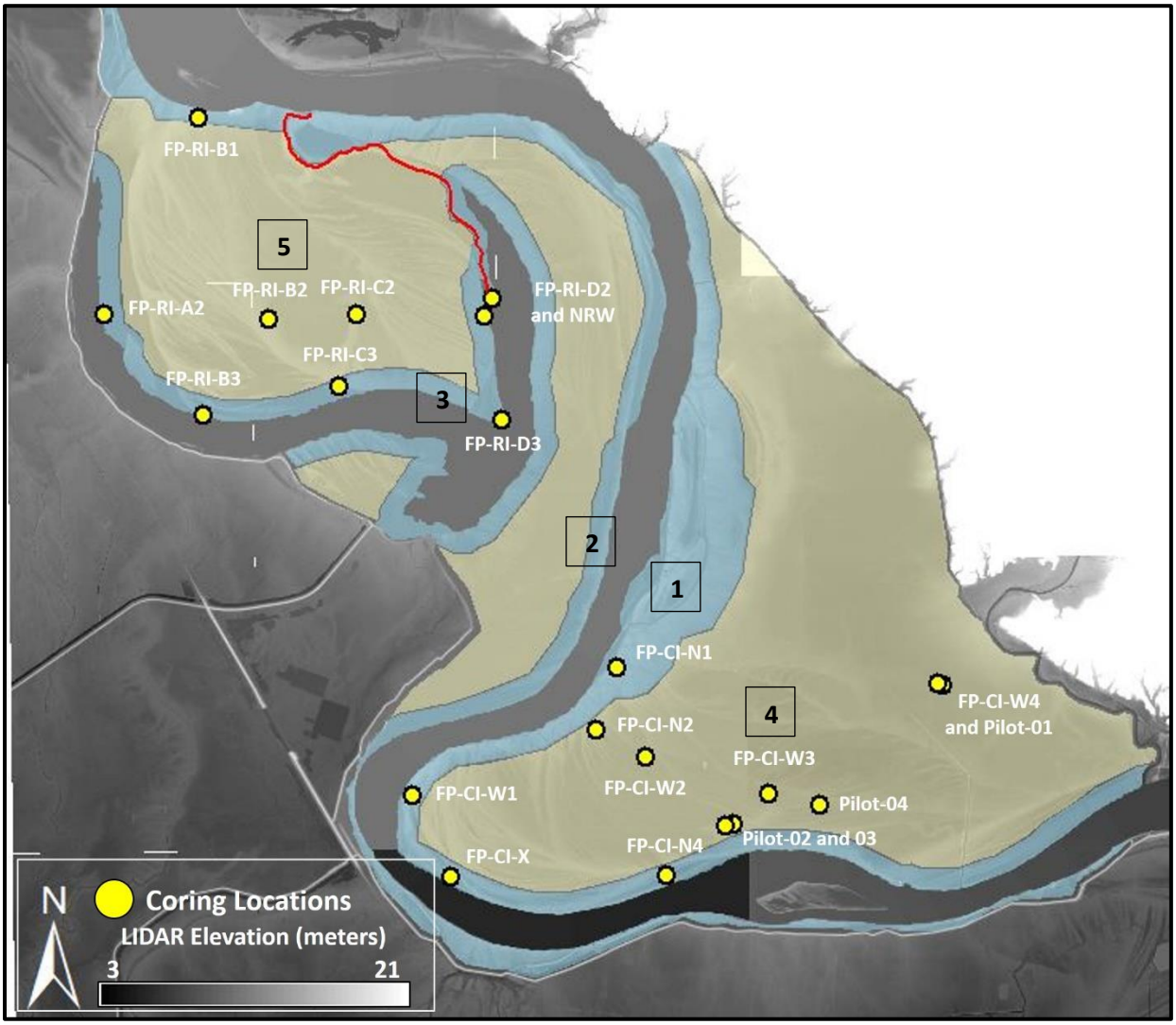


**Figure 33.** Sediment storage sinks in the study area include: 1) east bank, 2) west bank, 3) Raccourci Old River lakeshore (shaded in blue), 4) Cat Island, and 5) Raccourci Island (shaded in yellow).

### 4.4.1 Effects of Channel Proximity on Mass Accumulation Rates

Cores taken closer than 500 meters from an open water channel demonstrated an average mass accumulation rate of 0.769 g $cm^{-2}$. Analysis of the changing mass accumulation rates along the banks and lakeshore showed a weak correlation to increased distance with the mass accumulation

rate changing by 0.0028 g $cm^{-2}$ $yr^{-1}$ for every meter of increased distance from open water. Thus the following relationship can be applied:

*Mass Accumulation Rate (g $cm^{-2}$ $yr^{-1}$) =* (12)

*Channel Distance (horizontal meters) * 0.0028 (g $cm^{-2}$ $yr^{-1}$ (horizontal meters)$^{-1}$) + 0.274 (g $cm^{-2}$ $yr^{-1}$)*

This correlation ($r^2$ = 052) explained the most variability for this location of any regression explored.

**Table 13.** Near-channel core channel distances and mass accumulation rates

| Core Name | Distance from Channel (m) | MAR (g $cm^{-2}$ $y^{-1}$) |
|---|---|---|
| FP-CI-N1 | 392 | > 1.48 |
| FP-CI-N4 | 280 | 1.037 |
| FP-CI-X | 189 | 1.006 |
| FP-CI-W1 | 243 | 0.505 |
| FP-RI-A2 | 85 | 0.073 |
| FP-RI-B1 | 170 | 1.31 |
| FP-RI-B3 | 93 | 0.552 |
| FP-RI-C3 | 298 | 0.927 |
| FP-RI-D2 | 42 | 0.569 |
| FP-RI-D3 | 60 | > 0.255 |
| FP-RI-NRW | 110 | 0.744 |

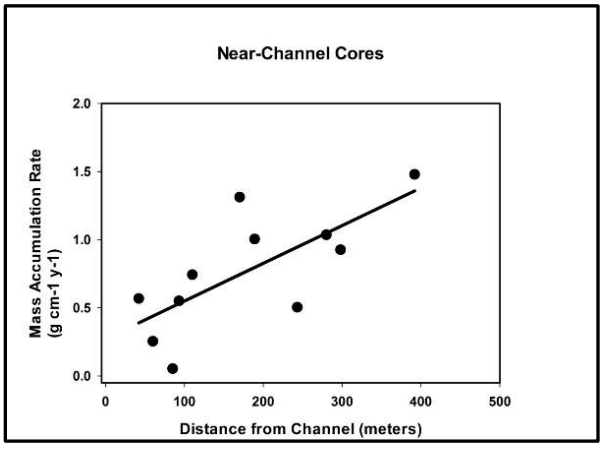


**Figure 34.** Analysis of the mass accumulation rates of cores taken near open water channels. MARs changed by 0.0028 g $cm^{-2}$ $y^{-1}$ for every meter of increased distance ($r^2$ = 0.52).

### 4.4.2 Effects of Elevation on Mass Accumulation Rates

Cores located on the main body of the point bars further inland than 500 meters have an average mass accumulation rate of 0.619 g $cm^{-2}$. The elevations for these locations ranged from 9.51 m to

12.68 m above mean sea level and represent the majority of cores collected at decreased elevations. The highest elevations in the study areas were the most proximal to the Mississippi River and Raccourci Old River. A regression elevation versus MAR was then created for cores beyond 500 meters from open water channels (Figure 35).

*Mass Accumulation Rate (g $cm^{-2}$ $yr^{-1}$) =* (13)

*Elevation (vertical meters) * 0.258 (g $cm^{-2}$ $yr^{-1}$ (vertical meters)$^{-1}$) – 2.25 (g $cm^{-2}$ $yr^{-1}$)*

The relationship between elevation and mass accumulation rates was much improved compared to any other factors ($r^2$ = 0.61). Initial hypotheses might have led to an expectation of increased mass accumulation rates at lower elevations. However, all of these cores were located away from the natural levees and the highest elevations in the study area. While these do not represent the absolute lowest elevations in the region, the cores can be classified on the lower end of elevation for the study area.

**Table 14.** Inland core elevations and mass accumulation rates.

| Core Name | Elevation (m) | MAR (g $cm^{-2}$ $y^{-1}$) |
|---|---|---|
| Pilot-01 | 9.51 | 0.31 |
| Pilot-02 | 12.62 | 1.11 |
| Pilot-03 | 11.20 | 0.61 |
| Pilot-04 | 10.30 | 0.41 |
| FP-CI-N2 | 11.37 | 0.231 |
| FP-CI-W2 | 10.38 | 0.582 |
| FP-CI-W3 | 11.09 | 0.617 |
| FP-CI-W4 | 9.89 | 0.206 |
| FP-RI-B2 | 12.11 | 1.28 |
| FP-RI-C2 | 12.68 | 0.841 |

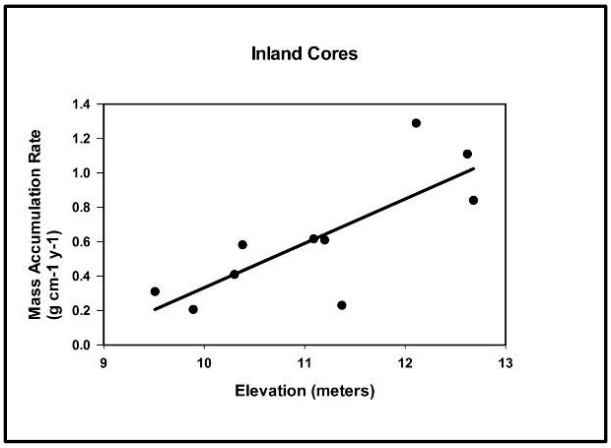


**Figure 35.** Analysis of the elevation versus mass accumulation rates of cores taken inland on the point bars. MARs changed by 0.258 g $cm^{-2}$ $y^{-1}$ for every meter of elevation gained ($r^2$ = 0.61).

### 4.5 Regional Mass Accumulation Rates ($MAR_R$) – Regression Analysis

Regression equations determined based on distance from open channel (Figure 34) and elevation (Figure 35) provide an alternative to simple spatial interpoloation, to estimate regional sediment accumulation. In order to apply the resulting mass accumulation rates at 1-$cm^2$ scale to the 5-$m^2$ scale pixels in the LIDAR data, each formula was multiplied by 250,000. Adding the individual mass accumulation rates assigned to each 5-$m^2$ pixel resulted in a value for each of the following storage sinks: Cat Island interior, Raccourci Island interior and near the Mississippi River and Raccourci Old River banks (Figure 33). The pixel values were then restricted to the polygon limits and counted using ERDAS Imagine to create a sum for each storage sink and the entire study area.

The total mass of sediment stored in the floodplain within 500 m of water banks and shores is 0.955 MT $yr^{-1}$ in an area encompassing 73 $km^2$ using the distance regression. Using the elevation regression, the total mass of sediment lost on the inland portions of the point bars is calculated to be 1.47 MT $yr^{-1}$ in an area encompassing 197 $km^2$. Combining these two estimates, the final regional mass accumulation rate was calculated to be 2.42 MT $yr^{-1}$ for the entire region encompassing 270 $km^2$ (Table 15). Uncertainty of $^{210}Pb$ age models and estimation of sample

volumes using from the gouge auger are each estimated at ~25%, yielding a range of regional floodplain sediment accumulation of 2.42 ± 0.61 MT $yr^{-1}$, or 1.81-3.03 MT $yr^{-1}$.

**Table 15.** Regional Mass Accumulation Rates along the Mississippi River floodplain based on experimental linear regressions.

| Storage Sink | Regression Type | Regional Mass Accumulation Rate (MT $yr^{-1}$) | Storage Sink Area ($km^2$) |
|---|---|---|---|
| Near Banks | Channel Distance | 0.955 | 73 |
| Cat Island Interior | Elevation | 0.631 | 113 |
| Raccourci Island Interior | Elevation | 0.839 | 84 |
| Total | N/A | 2.42 | 270 |

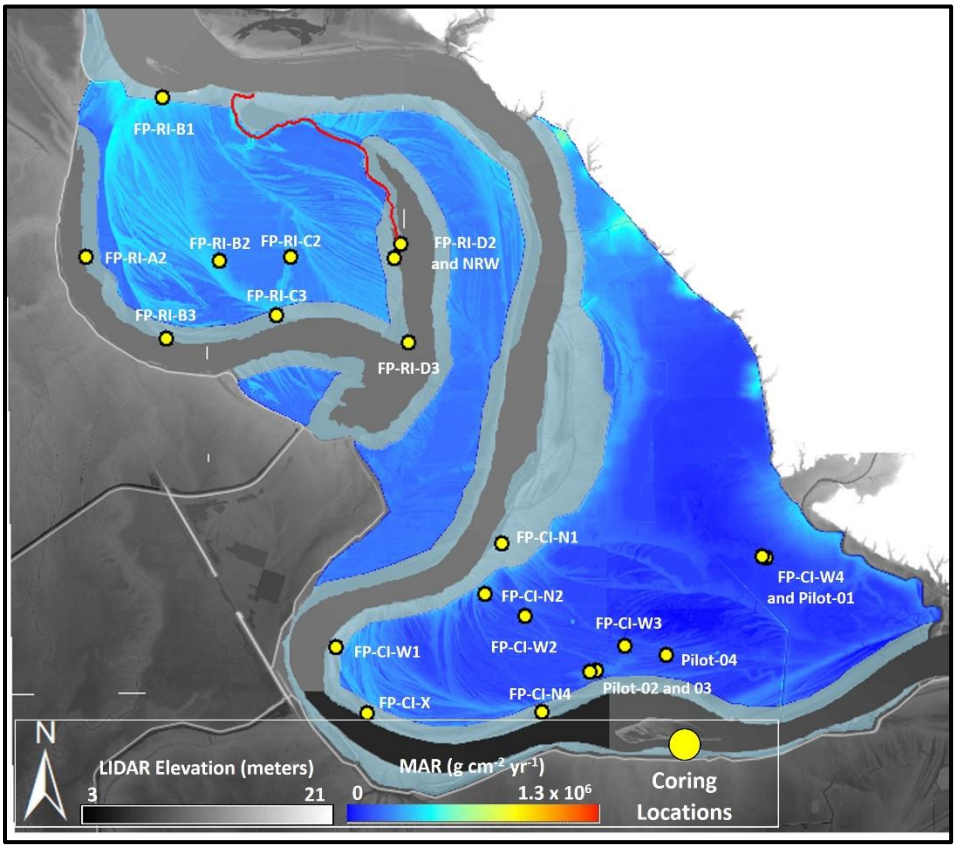


**Figure 36.** Based on elevation changes, these are the expected mass accumulation rates throughout the inland portions of the study area. The portions of the point bars nearest the Mississippi River and Raccourci Old River are highlighted in light blue. Results are included above in Table 16.

## 5. SUMMARY AND CONCLUSIONS

Though providing answers for refining the sediment budget in the major point bar complexes along this reach of the river, the scope of the study also creates a number of questions that are potentially unanswered. First this does not include inundated swales, as they were inaccessible during the field campaign. LIDAR imagery was able to pick up the elevation changes on the swale surfaces compared to the ridge surfaces, but it could not determine depths or the changing surface area of each swale.

Two additional areas for sediment storage exist within river levees, and outside of the region where cores were collected: the lacustrine delta of Raccourci Old River, and additional floodplains and islands between Saint Francisville and Baton Rouge (Table 16).

A study was conducted by Rowland, et al (2009) that addressed sediment deposition within and infilling of Raccourci Old River along and through The Narrows tie channel. Deposition in the lacustrine delta, deltaic growth, and infilling along banks of The Narrows continues today at a rate visible in overhead imagery over yearly timescales (Figure 37). Rowland, et al (2009) concluded that the dominant mechanism for the infilling of oxbow lakes was deposition from the river to the lake via the tie channel. Over the course of 147 years, from 1851-1998, Rowland, et al (2009) estimated that infilled lake volume was $5.7 \times 10^7$ $m^3$, accounting for a mass of 68 MT, at a rate of 0.45 MT $y^{-1}$ when using an assumed sediment density of 1.2 g $cm^{-3}$. Using the average dry mineral density applied to this study, 1.07 g $cm^{-3}$, this mass accumulation rate is estimated to be 0.40 MT $y^{-1}$. Thus infilling of Raccourci Old River accounts for an additional 0.4-0.45 MT $yr^{-1}$ lost from the Mississippi River and stored in the floodplain along the reach of the study area (Rowland, et al, 2005; Rowland, et al, 2009).

Between Saint Francisville and Baton Rouge, an additional 82$km^2$ of islands and floodplains exist that could capture flood sediment. In Table 16, $MAR_i$s are estimated using rates from natural

neighbor interpolation and uncertainty of 25%, yielding additional sediment capture of 0.639 ± 0.16 MT $yr^{-1}$.

Overall, our results yield estimated sediment capture within the floodplains of Cat Island and Raccourci Old River of 1.58-3.03 MT $yr^{-1}$; 1.98-3.48 MT $yr^{-1}$ for this region plus the lacustrine delta, all along the reach between Tarbert Landing and Saint Francisville; and extrapolated for all floodplain locations between Tarbert Landing and Baton Rouge plus the lacustrine delta, 2.46-4.27 MT $yr^{-1}$ (Table 16). These quantities include both sand and mud size fractions. For comparison, Allison et al. (2012) estimated that the masses of sediment lost from transport between Tarbert Landing and Saint Francisville are 15.9 MT $yr^{-1}$ of mud and 53.8 MT $yr^{-1}$ of sand for the years 2008-2010.

**Table 16.** Total sediment storage estimates. Total range of sediment storage is determined by adding the columns with asterisks (*) to each experimentally derived (1, 2) mass accumulation rate.

| Sediment Sink | Extrapolation of Natural Neighbor MAR (1) (MT $yr^{-1}$) | Regression Analysis MAR (2) (MT $yr^{-1}$) | Application of Natural Neighbor to Downstream Floodplains(*) (MT $yr^{-1}$) | Lacustrine Delta MAR(*) (MT $yr^{-1}$) (Rowland, et al, 2005) |
|---|---|---|---|---|
| Near Banks | ---- | 0.954 | ---- | ---- |
| Cat Island Interior | 1.08 | 0.631 | ---- | ---- |
| Raccourci Island Interior | 1.03 | 0.839 | ---- | ---- |
| Lacustrine Delta of the Narrows | ---- | ---- | ---- | 0.450 |
| Additional Floodplains | ---- | ---- | 0.639 | ---- |
| Method Sum | 2.11 ± 0.53 | 2.42 ± 0.61 | 0.639 ± 0.16 | 0.40-0.45 |
| Total | Study Area Floodplain Only: 1.58-3.03 MT $yr^{-1}$<br>All Locations: 2.46-4.27 MT $yr^{-1}$ | | | |

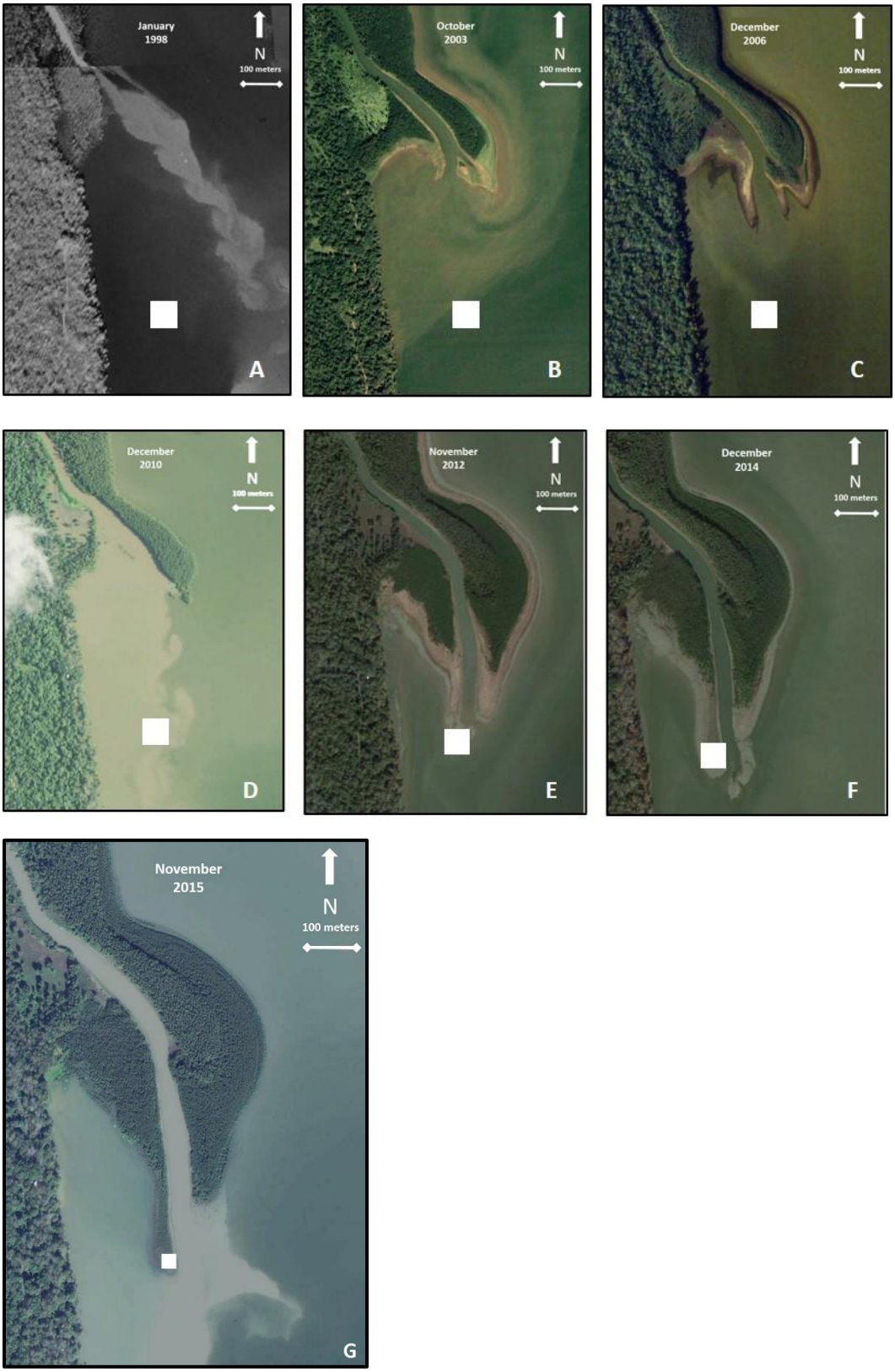
January
1998
N
100 meters
A
October
2003
N
100 meters
B
December
2006
N
100 meters
C
December
2010
N
100 meters
D
November
2012
N
100 meters
E
December
2014
N
100 meters
F
November
2015
N
100 meters
G

**Figure 37.** (a-f) Growth of The Narrows sand bar and lacustrine delta complex infills Raccourci Old River from 1998-2014. The square marker indicates the coring location of Core FP-RI-NRW. (g) The final overhead imagery frame, taken in November 2015, shows the impending emergence of the coring location above the surface of the lake.

Potential further studies along in this region could include bathymetric profiles of Raccourci Old River to determine total lake volume. A multi-site study of cores taken from the lake bed would also help explain additional sediment lost to these floodplains.

While total sediment loss has not been quantified above Tarbert Landing, additional point bar complexes exist in the reach of the Mississippi River that forms the border between Louisiana and Mississippi. Similar consideration of along that reach may aid in further sediment budget analysis.

## REFERENCES


1) Aalto, R., J. W. Lauer, and W. E. Dietrich, 2008, Spatial and temporal dynamics of sediment accumulation and exchange along Strickland River floodplains (Papua New Guinea) over decadal-to-centennial timescales, Journal of Geophysical Research, 113, F01S04, doi:10.1029/2006JF000627.

2) Allison, M.A., Demas, C.R., Ebersole, B.A. Kleiss, C.D. Little, E.A. Meselhe, N.J. Powell, Pratt, T.C., and Vosberg, B.M., 2012. A water and sediment budget for the lower Mississippi-Atchafalaya River in flood years 2008-2010: Implications for sediment discharge to the oceans and coastal restoration in Louisiana. Journal of Hydrology, Number 432, 84-97.

3) Appleby P.G., 2008. Three decades of dating recent sediments by fallout radionuclides: a review. The Holocene, Number 18, Volume 1, 83-93.

4) LSU Department of Geography and Anthropology, ATLAS: The Louisiana Statewide GIS. Retrieved from Atlas Louisiana GIS website, http://atlas.lsu.edu, accessed April 2017.

5) Bentley, S.J., Blum, M.D., Maloney, J., Pond, L., Paulsell, R., 2015. The Mississippi River source-to-sink system: Perspectives on tectonic, climatic, and anthropogenic influences, Miocene to Anthropocene. Earth-Science Reviews, Number 153, 139-174.

6) Blum, M.D. and Roberts, H.H., 2009. Drowning of the Mississippi delta due to insufficient sediment supply and global sea level rise. Nature Geoscience, Volume 2, 488-491.

7) Chmura, G.L., and Kosters, E.C. (1994) Storm deposition and $^{137}$Cs accumulation in fine-grained marsh sediments of the Mississippi Delta Plain. Estuarine, Coastal and Shelf Science, 39, 33–34.

8) Cochran, J.K and Masqué, P., 2003. Short-lived U/Th Series Radionuclides in the Ocean: Tracers for Scavenging Rates, Export Fluxes and Particle Dynamics. Reviews in Mineralogy and Geochemistry, Volume 52, Number 1, 461-492.

9) Corbett, D.R., and Walsh, J.P., 2015. $^{210}$Lead and $^{137}$Cesium: establishing a chronology for the last century. Handbook of Sea-Level Research, First Edition. Shennan, I., Long, A.J., and Horton, B.P., editors. Hoboken (NJ): John Wiley and Sons, Ltd.

10) Cutshall, N.H., Larsen, I.L., Olsen, C.R. (1983) Direct analysis of $^{210}$Pb in sediment samples: self-absorption corrections. Nuclear Instruments and Methods, 206, 1-20.

11) Day, J. W. Jr. et al., 2007. Restoration of the Mississippi Delta: Lessons from Hurricanes Katrina and Rita. Science, Issue 315, 1679-1684.

12) Hardy, E.P., 1971. Fallout program quarterly summary report with appendix. US Atomic Energy Commission, HASL-245, 255.

13) Heiri O., Lotter, A.F., Lemcke, G. (2001). Loss on ignition as a method for estimating organic and carbonate content in sediments: reproducibility and comparability of results. Journal of Paleolimnology, Volume 25, 101-110. Doi:10.1023/A.1008119611481.

14) Kesel, R. H., E.G. Yodis, D. McCraw., 1992. An approximation of the sediment budget of the lower Mississippi River prior to major human modification. Earth Surface Processes and Landforms, Volume 17, 711.

15) Louisiana Coastal Protection and Restoration Authority, 2017. Integrated ecosystem restoration and hurricane protection: Louisiana's comprehensive master plan for a sustainable coast. Retrieved from the Louisiana Coastal Protection and Restoration Authority website, http://coastal.la.gov/our-plan/2017-coastal-master-plan/, accessed April 2017.

16) Little, CD, and Biedenharn, DS, 2014, Mississippi River Hydrodynamic and Delta Management Study (MRHDM) – Geomorphic Assessment. US Army Corps of Engineers Report ERDC/CHL TR-14-5, 309

17) Muhammad, Z., Bentley, S.J., L. A. Febo, L.A., A. W. Droxler, A.W., G. R. Dickens, G.R., L. C. Peterson, L.C., and Opdyke, B.N., 2008. Excess $^{210}$Pb inventories and fluxes along the continental slope and basins of the Gulf of Papua, Journal of Geophysical Research, Number 113, F01S17, doi:10.1029/2006JF000676.

18) National Parks Service, Mississippi River Facts. Retrieved from the National Parks Service, https://www.nps.gov/miss/riverfacts.htm, accessed August 2017.

19) Nittrouer, C.A. and Sternberg, R.W., 1981. The formation of sedimentary strata in an allochthonous shelf environment: the Washington shelf. Marine Geology 42, 201-232.

20) Nittrouer, C.A., DeMaster, D.J., McKee, B.A., Cutshall, N.H. and Larson, I.L., 1983. The effect of sediment mixing on $^{210}$Pb accumulation rates for the Washington continental shelf. Marine Geology 54, 201-22.

21) Persac, Marie Adrien, Benjamin Moore Norman, and J.H. Colton & Co. Norman's chart of the lower Mississippi River. New Orleans, B. M. Norman, 1858. Map. Retrieved from the Library of Congress, https://www.loc.gov/item/78692178/, accessed June 2017.

22) Paola, C., R.R. Twilley, R.R., Edmonds, D.A., Kim, W. Mohrig, D., Parker, G., Viparelli, E. and Voller, V.R. (2010). Natural Processes in Delta Restoration: Application to the Mississippi Delta. Marine Sciences Annual Review 2011, Number 3, 67-91.

23) Ritchie, J. C., and J. R. McHenry. 1990. Application of Radioactive Fallout Cesium-137 for Measuring Soil Erosion and Sediment Accumulation Rates and Patterns: A Review. J. Environ. Qual. 19:215-233. doi:10.2134/jeq1990.00472425001900020006x

24) Rowland, J.C., Lepper, K., Dietrich, W.E., Wilson, C.J., Sheldon, R., 2005. Tie channel sedimentation rates, oxbow formation age and channel migration rate from optically stimulated luminescence (OSL) analysis of floodplain deposits. Earth Surface Processes and Landforms, Volume 30, 1161-1179.

25) Rowland, J.C., Dietrich, W.E., Day, G., Parker, G., 2009. Formation and maintenance of single-thread tie channels entering floodplain lakes: Observations from three diverse river systems. Journal of Geophysical Research, Volume 114, DOI: 10.1029/2008JF001073.

26) Smith, M., Bentley, S.J. (2014). Sediment capture in flood plains of the Mississippi River: A case study in Cat Island National Wildlife Refuge, Louisiana. Sediment Dynamics from the Summit to the Sea. IAHS Publication 367.

27) US Army Corps of Engineers New Orleans District. Station Information for Mississippi River at Red River Landing (01120). Retrieved from the US Army Corps of Engineers New Orleans District website, http://rivergages.mvr.usace.army.mil/WaterControl/stationinfo2.cfm?sid=01120&fid=&dt=S, accessed April 2017.

28) US Army Corps of Engineers, 2014. Morganza Floodway Interim Water Control Manual: Proposed Clarifications to the Standing Instructions. Retrieved from the US Army Corps of Engineers New Orleans District website, http://www.mvn.usace.army.mil/Portals/56/docs/MRT/MorganzaInterimWCMStandingInstructionsSimplifiedFINAL.pdf, accessed September 2017.

29) US Fish and Wildlife Service. Cat Island National Wildlife Refuge website. Retrieved from the US Fish and Wildlife Service website https://www.fws.gov/refuge/cat_island/, accessed August 2015.

30) Van de Lageweg, W.I., van Dijk, W.M., Baar, A.W., Rutten, J., Kleinhans, M.G. (2014). Bank pull or bar push: What drives scroll-bar formation in meandering rivers? Geology, Volume 42, Number 4, 319-322, doi:10.1130/G35192.1.

31) Van Dijk, W.M., Van de Lageweg, W.I., Kleinhans, M.G., 2013. Formation of a cohesive floodplain in a dynamic experimental meandering river. Earth Surface Processes and Landforms, Volume 38, 1550-1556, DOI: 10.1002/esp.3400

32) Wang, B. Xu, Y.J., 2015. Sediment Trapping by Emerged Channel Bars in the Lowermost Mississippi River during a Major Flood. Water, Issue 11, Number 5, 6079-6096, doi:10.3390/w7116079

**APPENDIX: Detailed tables for radioisotope activity, grain size analysis, and organic content**

**Core: FP-CI-N1**

| Depth (cm) | $^{210}$Pb Activity (dpm g-1) | $^{210}$Pb Error (dpm g-1) | $^{137}$Cs Activity (dpm g-1) | $^{137}$ Cs Error (dpm g$^{-1}$) | $D_{50}$ (μm) | Mineral Fraction (%) |
|---|---|---|---|---|---|---|
| 2 | -- | -- | 0 | 0 | 21.81 | 91 |
| 6 | -- | -- | 0 | 0 | 24.36 | 93 |
| 10 | -- | -- | 0.229 | 0.07 | 22.78 | 94 |
| 12 | -- | -- | 0.415 | 0.07 | 23.41 | 96 |
| 14 | -- | -- | 0.410 | 0.08 | 24.01 | 96 |
| 16 | -- | -- | 0.647 | 0.08 | 33.81 | 97 |
| 18 | -- | -- | 0.492 | 0.11 | 45.22 | 97 |
| 20 | -- | -- | 0.630 | 0.10 | 45.25 | 97 |
| 22 | -- | -- | 0.432 | 0.08 | 64.41 | 97 |
| 24 | -- | -- | 0.112 | 0.07 | 90.74 | 98 |
| 26 | -- | -- | 0 | 0 | 93.01 | 99 |
| 28 | -- | -- | 0 | 0 | 113.15 | 99 |
| 30 | -- | -- | 0 | 0 | 109.96 | 99 |
| 32 | -- | -- | 0 | 0 | 117.93 | 99 |
| 34 | -- | -- | 0 | 0 | 119.64 | 99 |
| 36 | -- | -- | 0 | 0 | 125.58 | 99 |
| 38 | -- | -- | 0 | 0 | 137.64 | 99 |
| 40 | -- | -- | 0 | 0 | 160.99 | 99 |
| 42 | -- | -- | 0 | 0 | 160.92 | 99 |
| 44 | -- | -- | 0 | 0 | 117.85 | 99 |
| 46 | -- | -- | 0 | 0 | 123.53 | 99 |
| 48 | -- | -- | 0 | 0 | 119.98 | 97 |
| 50 | -- | -- | 0 | 0 | 124.82 | 99 |
| 52 | -- | -- | 0 | 0 | 75.96 | 99 |
| 54 | -- | -- | 0 | 0 | 136.35 | 99 |
| 56 | -- | -- | 0.076 | 0.06 | 78.15 | 98 |
| 58 | -- | -- | 0.151 | 0.06 | 162.10 | 99 |
| 60 | -- | -- | 0.159 | 0.05 | 153.91 | 99 |
| 62 | -- | -- | 0 | 0 | 126.92 | 99 |
| 64 | -- | -- | 0 | 0 | 96.91 | 99 |
| 66 | -- | -- | 0.078 | 0.05 | 73.42 | 99 |

**Core: FP-CI-N2**

| Depth (cm) | $^{210}$Pb Activity (dpm g-1) | $^{210}$Pb Error (dpm g-1) | $^{137}$Cs Activity (dpm g-1) | $^{137}$ Cs Error (dpm g$^{-1}$) | $D_{50}$ (μm) | Mineral Fraction (%) |
|---|---|---|---|---|---|---|
| 2 | 2.894 | 0.24 | -- | -- | 8.89 | 86 |
| 4 | 3.371 | 0.24 | 0.151 | 0.09 | 8.42 | 86 |
| 6 | 2.000 | 0.18 | -- | -- | 7.48 | 87 |
| 8 | 0.653 | 0.06 | -- | -- | 6.19 | 94 |
| 10 | 2.007 | 0.16 | 0.435 | 0.11 | 6.49 | 95 |
| 12 | 1.280 | 0.07 | 0.280 | 0.10 | 5.56 | 95 |
| 14 | -- | -- | 0.354 | 0.10 | 5.64 | 95 |
| 16 | 0.039 | 0.01 | 0.449 | 0.09 | 7.92 | 96 |
| 18 | -- | -- | 0.916 | 0.13 | 6.58 | 97 |
| 20 | 0.218 | 0.02 | 1.289 | 0.12 | 1.015 | 97 |
| 22 | 0.028 | 0.01 | 1.199 | 0.12 | 10.71 | 97 |
| 24 | -- | -- | 1.001 | 0.12 | 13.67 | 96 |

**Core: FP-CI-N4**

| Depth (cm) | $^{210}$Pb Activity (dpm g-1) | $^{210}$Pb Error (dpm g-1) | $^{137}$Cs Activity (dpm g-1) | $^{137}$ Cs Error (dpm g$^{-1}$) | $D_{50}$ (μm) | Mineral Fraction (%) |
|---|---|---|---|---|---|---|
| 2 | -- | -- | -- | -- | 9.02 | 94 |
| 4 | 0.515 | 0.03 | 0.194 | 0.08 | 11.82 | 93 |
| 6 | 0.739 | 0.05 | -- | -- | 9.44 | 95 |
| 8 | 1.827 | 0.15 | -- | -- | 10.32 | 94 |
| 10 | 1.927 | 0.20 | 0.135 | 0.08 | 9.04 | 92 |
| 12 | 2.598 | 0.23 | 0.162 | 0.10 | 8.35 | 92 |
| 14 | 0.718 | 0.06 | 0.234 | 0.08 | 8.13 | 93 |
| 16 | 0.292 | 0.03 | 0.234 | 0.08 | 7.71 | 94 |
| 18 | 2.500 | 0.21 | -- | -- | 7.83 | 94 |
| 20 | 1.393 | 0.18 | 0.166 | 0.11 | 8.69 | 95 |
| 22 | 0.602 | 0.04 | 0.241 | 0.08 | 9.11 | 95 |
| 24 | 2.036 | 0.21 | 0.141 | 0.09 | 9.29 | 95 |
| 26 | 0.881 | 0.08 | 0.205 | 0.09 | 9.55 | 95 |
| 28 | -- | -- | 0.242 | 0.08 | 8.03 | 95 |
| 30 | -- | -- | 0.097 | 0.08 | 8.74 | 96 |
| 32 | -- | -- | 0.355 | 0.09 | 8.09 | 96 |
| 34 | -- | -- | 0.282 | 0.07 | 11.54 | 96 |
| 36 | -- | -- | 0.449 | 0.08 | 9.41 | 96 |
| 38 | -- | -- | 0.237 | 0.08 | 9.33 | 96 |
| 40 | -- | -- | 0.310 | 0.09 | 5.09 | 95 |
| 42 | -- | -- | 0.316 | 0.08 | 6.69 | 96 |
| 44 | 1.731 | 0.11 | 0.489 | 0.07 | 6.56 | 95 |
| 46 | -- | -- | 0.169 | 0.08 | 7.74 | 96 |
| 48 | 1.374 | 0.14 | 0.402 | 0.09 | 7.96 | 95 |
| 50 | 0.089 | 0.01 | 0.261 | 0.08 | 7.50 | 96 |
| 52 | -- | -- | 0.354 | 0.09 | 9.09 | 96 |
| 54 | -- | -- | 0.357 | 0.08 | 8.48 | 97 |
| 56 | -- | -- | 0.376 | 0.08 | 9.28 | 96 |
| 58 | 1.634 | 0.15 | 0.353 | 0.08 | 9.15 | 95 |
| 60 | 0.744 | 0.09 | 0.275 | 0.10 | 10.99 | 96 |

**Core: FP-CI-X**

| Depth (cm) | $^{210}$Pb Activity (dpm g-1) | $^{210}$Pb Error (dpm g-1) | $^{137}$Cs Activity (dpm g-1) | $^{137}$ Cs Error (dpm g$^{-1}$) | $D_{50}$ (μm) | Mineral Fraction (%) |
|---|---|---|---|---|---|---|
| 2 | 0.193 | 0.03 | 0.202 | 0.07 | 15.19 | 94 |
| 4 | 0.743 | 0.07 | 0.221 | 0.08 | 13.14 | 91 |
| 6 | 1.215 | 0.07 | 0.246 | 0.07 | 9.7 | 92 |
| 8 | 0.280 | 0.03 | 0.211 | 0.07 | 9.43 | 93 |
| 10 | 2.520 | 0.12 | 0.117 | 0.07 | .915 | 93 |
| 12 | 7.738 | 0.96 | -- | -- | 13.25 | 93 |
| 14 | 0.859 | 0.09 | -- | -- | 19.29 | 94 |
| 16 | 0.008 | 0.001 | 0.342 | 0.07 | 10.57 | 94 |
| 18 | 0.525 | 0.06 | 0.159 | 0.07 | 10.57 | 94 |
| 20 | -- | -- | 0.222 | 0.07 | 8.17 | 94 |
| 22 | 0.089 | 0.10 | 0.215 | 0.08 | -- | 95 |
| 24 | 0.507 | 0.05 | 0.329 | 0.08 | 10.99 | 95 |
| 26 | -- | -- | -- | -- | 11.82 | 95 |
| 28 | 0.643 | 0.07 | 0.193 | 0.08 | 8.06 | 95 |
| 30 | 0.080 | 0.01 | 0.319 | 0.07 | 12.53 | 94 |
| 32 | -- | -- | -- | -- | 15.09 | 94 |
| 34 | 0.168 | 0.02 | 0.403 | 0.08 | 11.20 | 94 |
| 36 | -- | -- | 0.233 | 0.08 | 10.19 | 94 |
| 38 | -- | -- | 0.378 | 0.09 | 9.99 | 94 |
| 40 | -- | -- | 0.361 | 0.07 | 9.99 | 94 |
| 42 | -- | -- | 0.346 | 0.08 | 10.32 | 94 |
| 44 | 0.437 | 0.04 | 0.342 | 0.08 | 14.65 | 95 |
| 46 | -- | -- | 0.386 | 0.08 | 14.66 | 95 |

**Core: FP-CI-W1**

| Depth (cm) | $^{210}$Pb Activity (dpm g-1) | $^{210}$Pb Error (dpm g-1) | $^{137}$Cs Activity (dpm g-1) | $^{137}$ Cs Error (dpm g$^{-1}$) | $D_{50}$ (μm) | Mineral Fraction (%) |
|---|---|---|---|---|---|---|
| 2 | 8.462 | 0.87 | -- | -- | 9.29 | 91 |
| 4 | 0.739 | 0.07 | 0.466 | 0.11 | 8.44 | 93 |
| 6 | 2.066 | 0.17 | -- | -- | 17.46 | 90 |
| 8 | 1.716 | 0.20 | -- | -- | 8.95 | 90 |
| 10 | 1.842 | 0.16 | -- | -- | 9.51 | -- |
| 12 | 0.812 | 0.10 | 0.256 | 0.09 | 9.68 | 95 |
| 14 | -- | -- | 0.499 | 0.10 | 12.59 | 97 |
| 16 | -- | -- | 0.663 | 0.10 | 17.24 | 97 |
| 18 | -- | -- | 0.619 | 0.09 | 32.60 | 95 |
| 20 | -- | -- | 1.069 | 0.11 | 25.68 | 96 |
| 22 | -- | -- | 1.232 | 0.12 | 30.92 | 97 |

**Core: FP-CI-W2**

| Depth (cm) | $^{210}$Pb Activity (dpm g-1) | $^{210}$Pb Error (dpm g-1) | $^{137}$Cs Activity (dpm g-1) | $^{137}$ Cs Error (dpm $g^{-1}$) | $D_{50}$ (μm) | Mineral Fraction (%) |
|---|---|---|---|---|---|---|
| 2 | 0.867 | 0.09 | 0.346 | 0.10 | 17.16 | 92 |
| 4 | 0.871 | 0.09 | -- | -- | 11.73 | 94 |
| 6 | 1.627 | 0.18 | -- | -- | 14.14 | 95 |
| 8 | -- | -- | -- | -- | 15.46 | 95 |
| 10 | -- | -- | -- | -- | 21.76 | 95 |
| 12 | 0.395 | 0.05 | 0.237 | 0.09 | 17.21 | 95 |
| 14 | -- | -- | 0.098 | 0.07 | 17.57 | 96 |
| 16 | 0.345 | 0.03 | 0.264 | 0.06 | 11.56 | 96 |
| 18 | 0.169 | 0.01 | 0.150 | 0.08 | 12.69 | 95 |
| 20 | 0.163 | 0.01 | 0.191 | 0.07 | 14.85 | 95 |
| 22 | 1.075 | 0.10 | 0.232 | 0.06 | 18.15 | 96 |
| 24 | -- | -- | 0.238 | 0.07 | 20.10 | 96 |
| 26 | -- | -- | 0.289 | 0.06 | 12.18 | 96 |
| 28 | -- | -- | 0.277 | 0.08 | 12.56 | 96 |
| 30 | 0.05 | 0.01 | 0.723 | 0.07 | 28.10 | 97 |
| 32 | 0.265 | 0.03 | 0.888 | 0.10 | 23.19 | 97 |
| 34 | -- | -- | 0.683 | 0.10 | 37.06 | 97 |
| 36 | -- | -- | 0.411 | 0.10 | 14.16 | 97 |
| 38 | -- | -- | 0.450 | 0.08 | 15.20 | 97 |
| 40 | -- | -- | 0.343 | 0.07 | 30.79 | 97 |

**Core: FP-CI-W3**

| Depth (cm) | $^{210}$Pb Activity (dpm g-1) | $^{210}$Pb Error (dpm g-1) | $^{137}$Cs Activity (dpm g-1) | $^{137}$ Cs Error (dpm g$^{-1}$) | $D_{50}$ (μm) | Mineral Fraction (%) |
|---|---|---|---|---|---|---|
| 2 | 1.041 | 0.10 | 0.211 | 0.12 | 12.45 | -- |
| 4 | 2.765 | 0.25 | 0.199 | 0.12 | 6.41 | -- |
| 6 | 1.142 | 0.11 | 0.315 | 0.11 | 8.89 | -- |
| 8 | 1.636 | 0.14 | 0.197 | 0.10 | 6.94 | -- |
| 10 | 3.729 | 0.24 | 0.175 | 0.07 | 6.08 | 90 |
| 12 | 2.295 | 0.19 | 0.194 | 0.06 | 6.34 | 93 |
| 14 | 0.523 | 0.03 | 0.283 | 0.07 | 73.0 | 94 |
| 16 | 0.719 | 0.07 | 0.313 | 0.08 | 6.36 | 94 |
| 18 | 0.532 | 0.03 | 0.398 | 0.08 | 6.13 | 94 |
| 20 | 0.969 | 0.10 | 0.413 | 0.09 | 6.67 | 94 |
| 22 | 0.308 | 0.04 | 0.298 | 0.06 | 6.89 | -- |
| 24 | 0.813 | 0.10 | 0.488 | 0.08 | 7.44 | 95 |
| 26 | 0.179 | 0.02 | 0.399 | 0.10 | 8.32 | 95 |
| 28 | 0.699 | 0.09 | 0.337 | 0.07 | 9.47 | 95 |
| 30 | 0.089 | 0.01 | 0.475 | 0.10 | 9.65 | 95 |
| 32 | 1.153 | 0.12 | 0.408 | 0.08 | -- | 95 |
| 34 | -- | -- | 0.401 | 0.09 | 7.92 | 95 |
| 36 | -- | -- | 0.559 | 0.09 | 8.84 | 95 |
| 38 | -- | -- | 1.478 | 0.12 | 13.43 | 96 |
| 40 | -- | -- | 0.878 | 0.11 | 12.72 | 96 |
| 42 | -- | -- | 0.189 | 0.09 | 11.22 | -- |
| 44 | -- | -- | 0.751 | 0.11 | 13.64 | 95 |
| 46 | -- | -- | 0.356 | 0.09 | 16.33 | 96 |
| 48 | -- | -- | 0.212 | 0.07 | 11.39 | 96 |
| 50 | 0.002 | 0.0003 | -- | -- | 19.23 | 95 |
| 52 | -- | -- | -- | -- | 8.66 | 97 |
| 54 | 0.192 | 0.03 | -- | -- | 27.93 | 97 |

**Core: FP-CI-W4**

| Depth (cm) | $^{210}$Pb Activity (dpm g-1) | $^{210}$Pb Error (dpm g-1) | $^{137}$Cs Activity (dpm g-1) | $^{137}$ Cs Error (dpm g$^{-1}$) | $D_{50}$ (μm) | Mineral Fraction (%) |
|---|---|---|---|---|---|---|
| 4 | -- | -- | 1.883 | 0.14 | 15.71 | 92 |
| 8 | -- | -- | 0.686 | 0.10 | 9.27 | 94 |
| 10 | -- | -- | 0.942 | 0.12 | 8.75 | 94 |
| 12 | -- | -- | 0.702 | 0.10 | 8.69 | 95 |
| 14 | -- | -- | 0.432 | 0.08 | 11.52 | 94 |

**Core: FP-RI-A2**

| Depth (cm) | $^{210}$Pb Activity (dpm g-1) | $^{210}$Pb Error (dpm g-1) | $^{137}$Cs Activity (dpm g-1) | $^{137}$ Cs Error (dpm $g^{-1}$) | $D_{50}$ (μm) | Mineral Fraction (%) |
|---|---|---|---|---|---|---|
| 2 | 8.749 | 0.41 | 0.343 | 0.07 | 6.35 | 72 |
| 4 | 5.486 | 0.32 | 0.302 | 0.07 | 8.73 | 75 |
| 6 | 5.100 | 0.28 | 1.494 | 0.10 | 4.65 | 77 |
| 8 | 3.557 | 0.28 | 2.684 | 0.14 | 4.93 | 88 |
| 10 | 1.516 | 0.11 | 0.642 | 0.06 | 4.69 | 95 |
| 12 | 1.662 | 0.15 | 0.195 | 0.04 | 5.12 | 95 |
| 14 | 1.698 | 0.14 | -- | -- | 4.77 | 96 |
| 16 | 0.950 | 0.08 | -- | -- | 5.09 | 95 |
| 18 | 1.885 | 0.13 | -- | -- | 4.00 | 95 |
| 20 | 2.031 | 0.14 | -- | -- | 4.23 | 95 |
| 22 | 2.031 | 0.07 | -- | -- | 6.35 | 95 |
| 24 | 0.845 | 0.17 | -- | -- | 4.38 | 96 |
| 26 | 0.597 | 0.06 | -- | -- | 4.31 | 97 |
| 28 | 1.202 | 0.11 | -- | -- | -- | 97 |

**Core: FP-RI-B1**

| Depth (cm) | $^{210}$Pb Activity (dpm g-1) | $^{210}$Pb Error (dpm g-1) | $^{137}$Cs Activity (dpm g-1) | $^{137}$ Cs Error (dpm g$^{-1}$) | $D_{50}$ (μm) | Mineral Fraction (%) |
|---|---|---|---|---|---|---|
| 2 | 1.861 | 0.16 | -- | -- | 49.01 | 98 |
| 4 | -- | -- | -- | -- | 63.72 | 98 |
| 6 | -- | -- | -- | -- | 39.60 | 98 |
| 8 | -- | -- | -- | -- | 43.68 | 97 |
| 10 | -- | -- | -- | -- | 65.85 | 97 |
| 12 | 1.425 | 0.12 | -- | -- | 67.06 | 98 |
| 14 | -- | -- | -- | -- | 73.50 | 96 |
| 16 | -- | -- | -- | -- | 116.012 | 98 |
| 18 | 0.744 | 0.08 | 0.074 | 0.03 | 101.10 | 99 |
| 20 | -- | -- | -- | -- | 9.03 | 99 |
| 22 | -- | -- | -- | -- | 96.93 | 99 |
| 24 | -- | -- | -- | -- | 73.89 | 98 |
| 26 | 1.121 | 0.10 | 0.101 | 0.03 | 55.58 | 99 |
| 28 | 0.961 | 0.08 | -- | -- | 47.76 | 98 |
| 30 | 0.821 | 0.09 | -- | -- | 59.04 | 98 |
| 32 | 1.137 | 0.10 | -- | -- | -- | 98 |
| 34 | 0.841 | 0.08 | -- | -- | 75.55 | 99 |
| 36 | 1.089 | 0.10 | 0.028 | 0.03 | 67.77 | 98 |
| 38 | 2.058 | 0.14 | 0.077 | 0.03 | 37.09 | 97 |
| 40 | 1.579 | 0.12 | 0.099 | 0.03 | 28.32 | 98 |
| 42 | 0.633 | 0.07 | 0.058 | 0.04 | 68.79 | 98 |
| 44 | 0.821 | 0.08 | -- | -- | 89.92 | 99 |
| 46 | 0.841 | 0.08 | -- | -- | 75.25 | 99 |
| 48 | 0.950 | 0.04 | 0.095 | 0.02 | 58.79 | 98 |
| 50 | 1.591 | 0.12 | -- | -- | 37.10 | 98 |
| 52 | 1.295 | 0.11 | -- | -- | 50.46 | 99 |
| 54 | 1.154 | 0.10 | 0.052 | 0.02 | 45.59 | 99 |
| 56 | 1.238 | 0.10 | -- | -- | 47.01 | 98 |
| 58 | 1.379 | 0.11 | 0.043 | 0.03 | 27.85 | 98 |
| 60 | 0.996 | 0.09 | 0.062 | 0.03 | 25.07 | 98 |

**Core: FP-RI-B2**

| Depth (cm) | $^{210}$Pb Activity (dpm g-1) | $^{210}$Pb Error (dpm g-1) | $^{137}$Cs Activity (dpm g-1) | $^{137}$ Cs Error (dpm g$^{-1}$) | $D_{50}$ (μm) | Mineral Fraction (%) |
|---|---|---|---|---|---|---|
| 2 | 24.02 | 0.57 | 0.938 | 0.12 | 5.67 | 90 |
| 4 | -- | -- | -- | -- | 5.63 | 90 |
| 6 | -- | -- | -- | -- | 6.34 | 90 |
| 8 | 28.99 | 0.66 | 0.898 | 0.15 | 5.33 | 89 |
| 10 | 61.25 | 1.38 | 1.311 | 0.24 | 5.41 | 91 |
| 12 | 13.45 | 0.10 | 1.329 | 0.09 | 5.84 | 92 |
| 14 | 22.25 | 0.64 | 1.197 | 0.09 | 5.76 | 93 |
| 16 | 16.08 | 0.37 | 0.874 | 0.09 | 5.66 | 94 |
| 18 | 13.79 | 0.33 | 0.61 | 0.07 | 5.79 | 92 |
| 20 | 16.04 | 0.38 | 0.465 | 0.08 | 5.46 | 94 |
| 22 | 11.72 | 0.29 | 0.244 | 0.05 | 5.58 | 95 |
| 24 | -- | -- | -- | -- | 5.46 | 95 |
| 26 | 19.64 | 0.54 | 0.155 | 0.06 | 6.69 | 94 |
| 28 | 20.46 | 0.56 | -- | -- | 4.82 | 95 |
| 30 | 14.38 | 0.34 | -- | -- | 4.83 | 95 |
| 32 | 21.29 | 0.59 | 0.172 | 0.05 | 4.98 | 92 |
| 34 | 13.92 | 0.32 | -- | -- | 5.17 | 94 |
| 36 | 1.868 | 0.05 | -- | -- | 5.51 | 95 |
| 38 | 10.53 | 0.28 | -- | -- | 5.91 | 96 |
| 40 | 18.83 | 0.55 | -- | -- | 9.27 | 96 |
| 42 | 13.23 | 0.04 | 0.101 | 0.05 | 5.24 | 96 |
| 44 | 20.89 | 0.35 | -- | -- | 8.44 | 96 |
| 46 | 14.27 | 0.43 | -- | -- | 8.88 | 96 |
| 48 | 16.79 | 0.41 | -- | -- | 7.79 | 96 |
| 50 | -- | -- | -- | -- | 6.22 | 96 |
| 52 | -- | -- | -- | -- | 7.81 | 96 |
| 54 | 22.21 | 0.63 | 0.315 | 0.07 | 7.16 | 97 |
| 56 | 14.63 | 0.35 | 0.121 | 0.06 | 5.09 | 97 |
| 58 | 16.15 | 0.38 | -- | -- | 9.46 | 97 |
| 60 | 23.60 | 0.61 | 0.121 | 0.04 | 8.85 | 97 |
| 62 | 21.39 | 0.56 | 0.099 | 0.04 | 7.94 | 97 |
| 64 | 22.42 | 0.61 | -- | -- | 12.25 | 97 |
| 66 | 17.13 | 0.76 | -- | -- | 13.17 | 97 |

**Core: FP-RI-B3**

| Depth (cm) | $^{210}$Pb Activity (dpm g-1) | $^{210}$Pb Error (dpm g-1) | $^{137}$Cs Activity (dpm g-1) | $^{137}$ Cs Error (dpm g$^{-1}$) | $D_{50}$ (μm) | Mineral Fraction (%) |
|---|---|---|---|---|---|---|
| 2 | 1.628 | 0.16 | 0.113 | 0.05 | 67.47 | 89 |
| 4 | 1.418 | 0.14 | 0.116 | 0.05 | 64.94 | 97 |
| 6 | 1.149 | 0.11 | 0.079 | 0.04 | 70.31 | 97 |
| 8 | 0.890 | 0.08 | 0.0957 | 0.03 | 73.10 | 98 |
| 10 | 1.192 | 0.10 | 0.048 | 0.03 | 73.38 | 98 |
| 12 | 0.659 | 0.08 | -- | -- | 69.57 | 98 |
| 14 | 0.651 | 0.07 | 0.060 | 0.03 | 64.09 | 98 |
| 16 | 0.775 | 0.08 | -- | -- | 65.19 | 98 |
| 18 | 00781 | 0.08 | -- | -- | 64.09 | 98 |
| 20 | 0.922 | 0.08 | -- | -- | 66.41 | 98 |
| 22 | 0.818 | 0.09 | -- | -- | 65.43 | 98 |
| 24 | 0.630 | 0.07 | -- | -- | 64.42 | 98 |
| 26 | 0.060 | 0.01 | -- | -- | 72.13 | 98 |

**Core: FP-RI-C2**

| Depth (cm) | $^{210}$Pb Activity (dpm g-1) | $^{210}$Pb Error (dpm g-1) | $^{137}$Cs Activity (dpm g-1) | $^{137}$ Cs Error (dpm g$^{-1}$) | $D_{50}$ (μm) | Mineral Fraction (%) |
|---|---|---|---|---|---|---|
| 2 | 22.58 | 0.93 | 0.403 | 0.08 | 20.18 | 94 |
| 4 | 25.06 | 0.99 | 0.247 | 0.08 | 7.91 | 94 |
| 6 | 15.83 | 0.68 | 0.705 | 0.08 | 6.91 | 94 |
| 8 | 34.31 | 0.84 | 0.737 | 0.10 | 6.36 | -- |
| 10 | 28.74 | 0.72 | 0.569 | 0.09 | 5.34 | 92 |
| 12 | -- | -- | -- | -- | 6.09 | -- |
| 14 | 25.35 | 0.66 | 0.594 | 0.08 | 5.88 | 92 |
| 16 | 15.49 | 0.86 | 0.416 | 0.07 | 5.97 | 95 |
| 18 | 14.25 | 0.34 | -- | -- | 6.26 | 95 |
| 20 | -- | -- | -- | -- | 7.98 | -- |
| 22 | 22.79 | 0.56 | 0.134 | 0.06 | 17.77 | 95 |
| 24 | 18.45 | 0.47 | 0.190 | 0.06 | 20.77 | 96 |
| 26 | 16.74 | 0.42 | 0.068 | 0.04 | 22.47 | -- |
| 28 | 17.33 | 0.42 | -- | -- | 9.76 | 96 |
| 30 | 17.69 | 0.45 | -- | -- | 24.59 | 97 |

**Core: FP-RI-C3**

| Depth (cm) | $^{210}$Pb Activity (dpm g-1) | $^{210}$Pb Error (dpm g-1) | $^{137}$Cs Activity (dpm g-1) | $^{137}$ Cs Error (dpm g$^{-1}$) | $D_{50}$ (μm) | Mineral Fraction (%) |
|---|---|---|---|---|---|---|
| 2 | 2.938 | 0.21 | 0.430 | 0.06 | 7.31 | 98 |
| 4 | -- | -- | -- | -- | 10.51 | 99 |
| 6 | -- | -- | -- | -- | 7.49 | 98 |
| 8 | -- | -- | -- | -- | 7.27 | 97 |
| 10 | -- | -- | -- | -- | 2.28 | 98 |
| 12 | 1.792 | 0.14 | 0.530 | 0.06 | 8.45 | 97 |
| 14 | 1.933 | 0.18 | 0.148 | 0.06 | 8.15 | 97 |
| 16 | 1.176 | 0.11 | 0.271 | 0.05 | 11.04 | 98 |
| 18 | 1.103 | 0.10 | 0.414 | 0.05 | 8.39 | 99 |
| 20 | 1.029 | 0.10 | 0.509 | 0.06 | 8.02 | 98 |
| 22 | 1.455 | 0.13 | 0.758 | 0.05 | 7.25 | 97 |
| 24 | 0.796 | 0.07 | 0.146 | 0.05 | 31.37 | 99 |
| 26 | 0.947 | 0.10 | 0.097 | 0.04 | 42.88 | 99 |
| 28 | 0.430 | 0.05 | 0.073 | 0.03 | 28.95 | 99 |
| 30 | 0.181 | 0.02 | -- | -- | 28.01 | 99 |
| 32 | 0.177 | 0.02 | -- | -- | 43.13 | 99 |
| 34 | 1.136 | 0.10 | -- | -- | 42.19 | 99 |
| 36 | 0.902 | 0.08 | -- | -- | 43.59 | 99 |
| 38 | 0.162 | 0.02 | -- | -- | 42.69 | 99 |
| 40 | 1.566 | 0.13 | -- | -- | 45.81 | 99 |
| 42 | 0.272 | 0.3 | -- | -- | 42.13 | 99 |
| 44 | 1.083 | 0.10 | -- | -- | 42.53 | 99 |
| 46 | 0.710 | 0.07 | -- | -- | 42.89 | 99 |
| 48 | 0.569 | 0.06 | -- | -- | 45.01 | 99 |
| 50 | 1.170 | 0.12 | -- | -- | 36.08 | 99 |

**Core: FP-RI-D2**

| Depth (cm) | $^{210}$Pb Activity (dpm g-1) | $^{210}$Pb Error (dpm g-1) | $^{137}$Cs Activity (dpm g-1) | $^{137}$ Cs Error (dpm g$^{-1}$) | $D_{50}$ (μm) | Mineral Fraction (%) |
|---|---|---|---|---|---|---|
| 2 | 6.663 | 0.33 | 0.836 | 0.08 | 5.29 | 84 |
| 4 | -- | -- | -- | -- | 8.89 | 85 |
| 6 | -- | -- | -- | -- | 6.05 | 86 |
| 8 | 4.568 | 0.31 | 0.735 | 0.08 | 6.74 | 90 |
| 10 | 2.791 | 0.18 | 0.657 | 0.07 | 5.10 | 90 |
| 12 | 2.475 | 0.17 | 0.600 | 0.05 | 6.29 | 93 |
| 14 | 1.786 | 0.17 | 0.464 | 0.06 | 8.98 | 93 |
| 16 | 1.129 | 0.10 | 0.252 | 0.06 | 9.37 | 93 |
| 18 | 1.219 | 0.13 | 0.206 | 0.06 | 10.98 | 95 |
| 20 | 1.561 | 0.14 | -- | -- | 10.67 | 96 |
| 22 | 0.571 | 0.06 | 0.081 | 0.04 | 9.56 | 97 |
| 24 | 1.048 | 0.19 | 0.275 | 0.06 | 10.14 | 96 |
| 26 | 0.795 | 0.07 | 0.373 | 0.05 | 8.11 | 96 |
| 28 | 0.711 | 0.06 | 0.234 | 0.04 | 21.98 | 97 |
| 30 | 0.042 | 0.01 | 0.127 | 0.04 | 25.23 | 97 |
| 32 | 1.690 | 0.15 | -- | -- | 34.01 | 98 |
| 34 | 0.569 | 0.07 | 0.059 | 0.03 | 37.92 | 96 |
| 36 | 13.41 | 0.13 | -- | -- | 43.29 | 96 |
| 38 | 0.992 | 0.08 | -- | -- | 53.97 | 97 |
| 40 | 0.546 | 0.06 | 0.064 | 0.03 | 72.29 | 96 |
| 42 | 0.490 | 0.06 | -- | -- | 60.19 | 98 |
| 44 | 1.103 | 0.12 | -- | -- | 53.73 | 98 |
| 46 | 0.554 | 0.06 | -- | -- | 62.37 | 98 |
| 48 | 0.969 | 0.10 | -- | -- | 51.53 | 98 |
| 50 | 0.218 | 0.03 | -- | -- | 67.06 | 98 |
| 52 | 0.196 | 0.02 | -- | -- | 49.33 | 98 |

**Core: FP-RI-D3**

| Depth (cm) | $^{210}$Pb Activity (dpm g-1) | $^{210}$Pb Error (dpm g-1) | $^{137}$Cs Activity (dpm g-1) | $^{137}$ Cs Error (dpm g$^{-1}$) | $D_{50}$ (μm) | Mineral Fraction (%) |
|---|---|---|---|---|---|---|
| 4 | 27.26 | 0.73 | 1.249 | 0.10 | 4.62 | 92 |
| 6 | 22.21 | 0.64 | 0.583 | 0.09 | 3.55 | 93 |
| 8 | 13.76 | 0.33 | 0.206 | 0.07 | 3.43 | 92 |
| 10 | 15.84 | 0.37 | 0.171 | 0.06 | 3.55 | 93 |
| 12 | 12.89 | 0.32 | 0.135 | 0.06 | 3.29 | 94 |
| 14 | 19.08 | 0.58 | 0.080 | 0.06 | 4.68 | 95 |
| 16 | 17097 | 0.41 | 0.251 | 0.07 | 4.59 | 95 |
| 18 | 21.56 | 0.59 | -- | -- | 4.12 | 95 |
| 20 | 22.22 | 0.62 | 0.130 | 0.07 | 3.45 | 94 |

**Core: FP-RI-NRW**

| Depth (cm) | $^{210}$Pb Activity (dpm g-1) | $^{210}$Pb Error (dpm g-1) | $^{137}$Cs Activity (dpm g-1) | $^{137}$ Cs Error (dpm $g^{-1}$) | $D_{50}$ (μm) | Mineral Fraction (%) |
|---|---|---|---|---|---|---|
| 2 | 8.824 | 0.72 | -- | -- | 25.47 | 98 |
| 4 | 2.443 | 0.18 | 0.112 | 0.04 | 31.20 | 98 |
| 6 | 2.546 | 0.18 | 0.162 | 0.04 | 24.59 | 98 |
| 8 | 2.420 | 0.17 | 0.117 | 0.04 | 26.03 | 97 |
| 10 | 2.833 | 0.21 | 0.107 | 0.04 | -- | 97 |
| 12 | 1.859 | 0.14 | 0.083 | 0.02 | 25.46 | 98 |
| 14 | 3.284 | 0.22 | -- | -- | 27.14 | 98 |
| 16 | 2.344 | 0.17 | 0.068 | 0.03 | 36.40 | 98 |
| 18 | 2.750 | 0.19 | 0.068 | 0.03 | 31.02 | 98 |
| 20 | 2.699 | 0.19 | -- | -- | 21.59 | 97 |
| 22 | 3.109 | 0.21 | 0.79 | 0.04 | 28.91 | 97 |
| 24 | 1.637 | 0.13 | -- | -- | 42.11 | 97 |
| 26 | 2.247 | 0.17 | 0.051 | 0.04 | 21.58 | 98 |
| 28 | 3.185 | 0.20 | -- | -- | 30.14 | 97 |
| 30 | 1.662 | 0.14 | -- | -- | 23.82 | 98 |
| 32 | 1.429 | 0.13 | -- | -- | 37.99 | 98 |
| 34 | 2.106 | 0.16 | -- | -- | 32.07 | 98 |
| 36 | 2.157 | 0.15 | 0.044 | 0.04 | 35.64 | 98 |
| 38 | 1.308 | 0.13 | -- | -- | 32.89 | 98 |

## VITA

Christopher Ryan Magliolo is a native of Hammond, Louisiana, where he resides with his wife Sarah, and their four children – Braden, Ian, Ava Sophia, and Augustin. He received a bachelor of science in Geology from Louisiana State University in August 2015. Prior to beginning his studies in geology, he completed a degree in Biological Sciences from Louisiana State University in May 2002. Following the outbreak of worldwide hostilities, he served more than nine years, from 2003-2013, on active duty as a United States Marine. During his service, he received an Associate of Arts in Arabic Language Studies from the Defense Language Institute – Foreign Language Center in Monterey, California. He is a graduate of the Basic Reconnaissance Course. Operationally, he has served in the intelligence, reconnaissance, and special operations communities, including two deployments to Afghanistan in support of Operation Enduring Freedom. He continues to serve in the Marine Corps Reserve and holds the reserve rank of Gunnery Sergeant of Marines. He is currently a force reconnaissance team leader at 3$^{d}$ Force Reconnaissance Company, 4$^{th}$ Marine Division, Marine Forces Reserve. His anticipated graduation is December 2017, and he plans to begin a career in the oil and gas industry in the coming months.